Remote Sensing of Environment 115 (2011) 2302–2319

Contents lists available at ScienceDirect

Remote Sensing of Environment

journal homepage: www.elsevier.com/locate/rse

Continental-scale net radiation and evapotranspiration estimated using MODIS satellite observations

Yufang Jin [a,b,*], James T. Randerson [a], Michael L. Goulden [a]

[a] Department of Earth System Science, University of California, Irvine, CA 92697, USA
[b] Joint Institute for Regional Earth System Science and Engineering, University of California, Los Angeles, CA 90095, USA

ARTICLE INFO

Article history:
Received 3 February 2011
Received in revised form 17 April 2011
Accepted 23 April 2011
Available online 2 June 2011

Keywords:
Regional evapotranspiration
Remote sensing
Radiation
Optimization
Gradient
AmeriFlux

ABSTRACT

Evapotranspiration (ET) is a major pathway for water loss from many ecosystems, and its seasonal variation affects soil moisture and net ecosystem CO_2 exchange. We developed an algorithm to estimate ET using a semi-empirical Priestley–Taylor (PT) approach, which can be applied at a range of spatial scales. We estimated regional net radiation (R_{net}) at monthly time scales using MODerate resolution Imaging Spectroradiometer (MODIS) albedo and land surface temperature. Good agreement was found between satellite-based estimates of monthly R_{net} and field-measured R_{net}, with a RMSE of less than 30 W m^{-2}. An adjustable PT coefficient was parameterized as a function of leaf area index and soil moisture based on observations from 27 AmeriFlux eddy covariance sites. The biome specific optimization using tower-based observations performed well, with a RMSE of 17 W m^{-2} and a correlation of 0.90 for predicted monthly latent heat. We implemented the approach within the hydrology module of the CASA biogeochemical model, and used it to estimate ET at a 1 km spatial resolution for the conterminous United States (CONUS). The RMSE of modeled ET was reduced to 21.1 mm mon^{-1}, compared to 27.1 mm mon^{-1} in the original CASA model. The monthly ET rates averaged over the Mississippi River basin were similar to those derived using GRACE satellite measurements and river discharge data. ET varied substantially over the CONUS, with annual mean values of 110 ± 76 mm yr^{-1} in deserts, 391 ± 176 mm yr^{-1} in savannas and grasslands, and 840 ± 234 mm yr^{-1} in broadleaf forests. The PT coefficient was the main driver for the spatial variation of ET in arid areas, whereas R_{net} controlled ET when mean annual precipitation was higher than approximately 400 mm yr^{-1}.

1. Introduction

Average annual evapotranspiration (ET) from the global land surface is around 60 to 65% of precipitation (Baumgartner & Reichel, 1975). ET is an important flux that links water, carbon, and energy (Campbell & Norman, 1998). Together with precipitation and runoff, ET governs water availability, and plays a key role in water resource planning and management. Available water resources are being tapped close to the limit in many parts of the world, and accurate estimates of the consumptive use of water through ET are needed. Annual ET is approximately equal to precipitation when averaged over many years in hot arid environments, whereas it is regulated primarily by available energy in humid environments (Choudhury & DiGirolamo, 1998).

Various distributed hydrological models and land surface parameterization schemes have been developed to quantify and predict regional ET flux (Overgaard et al., 2006). Recent efforts to improve regional ET estimates make use of the spatial and temporal coverage of satellite observations of vegetation properties and surface temperature. A common approach is based on the land surface energy balance (SEB), either to calculate latent heat as the residual of SEB by subtracting sensible heat from available energy, or to estimate evaporative fraction (EF). Main operational approaches include the Resistance Surface Energy Balance (Kalma & Jupp, 1990), the Surface Energy Balance Algorithm for Land (SEBAL) (Bastiaanssen et al., 1998a; Bastiaanssen et al., 1998b), and the Surface Energy Balance System (SEBS) (Su, 2002). The calculation of sensible heat flux from remote sensing data is sensitive to the accuracy of the estimated difference between surface and air temperature and is limited by estimates of aerodynamic resistance. On the other hand, using EF estimated from satellite images has the advantage of reducing the complexity related to the determination of sensible heat. The "triangle-method" has been developed to estimate EF using the diagram of surface radiant temperature (T_s) and vegetation index (VI) (Jiang & Islam, 2001; Nishida et al., 2003). It is based on the scatterplots of VI and T_s for all pixels in a satellite image which are typically bounded by a triangle with vertices representing the dry and

---

* Corresponding author at: 3317 Croul Hall, Department of Earth System Science, University of California at Irvine, Irvine, CA 92697-3100, USA. Tel.: +1 949 824 0597; fax: +1 949 824 3874.
E-mail address: yufang@uci.edu (Y. Jin).

0034-4257/$ – see front matter © 2011 Elsevier Inc. All rights reserved.
doi:10.1016/j.rse.2011.04.031

wet bare soil and full-cover vegetation (Gillies et al., 1997). SEB terms for the extreme cases (e.g., completely wet or dry pixels) can be either estimated from ground data or resolved from physically-based models, allowing linear interpolation to all pixels. Another similar method estimates EF using the diagram of LST and broadband albedo from satellite images without the use of field data (Bastiaanssen et al., 1998a; Bastiaanssen et al., 1998b; Roerink et al., 2000; Verstraeten et al., 2005, 2008). However, deriving surface parameters from the vertex of VI–T_s or LST-albedo scatterplots requires a continuum of soil moisture and vegetation status to provide a range of surface conditions, and many parameters are required to resolve the end-member SEB terms. These methods are usually calibrated for specific regions; their robustness across multiple regions has not been systematically evaluated.

Environmental and biophysical controls play important roles in regulating ET on diurnal to interannual time scales (Baldocchi et al., 2004; Baldocchi & Xu, 2007; Ryu et al., 2008). Statistical empirical models have been developed to upscale the ground-based flux data to regional scales by building statistical relationships between field measured ET and a suite of environmental and satellite derived vegetation properties (Nagler et al., 2005). Dahm et al. (2002) present evidence that the best predictor of ET in a semi-arid drainage basin is leaf area index (LAI), and the relationship appears to hold across species during periods with limited or no water stress. Surface resistance increases and the response of different species diverges with increasing water or salt stress (Nagler et al., 2003). These empirical relationships were developed from a limited number of sites and their application to other ecosystems requires validation. Machine learning techniques have also been trained with networks of ground-based observations to predict ET at regional or continental scales based on meteorological data and remotely sensed vegetation properties (Jung et al., 2009; Jung et al., 2010; Lu & Zhuang, 2010; Yang et al., 2006). An important challenge with these approaches is understanding the mechanisms by which key driving variables interact, thus enabling use of the models to extrapolate fluxes to past and future periods.

The Penman–Monteith (PM) equation (Monteith, 1965) is a well-accepted physically-based formulation for estimating ET that combines energy and aerodynamic considerations. It requires information on available energy, air temperature, humidity, wind speed, and surface and canopy aerodynamic resistance. Recent work has focused on developing generalized parameterizations for canopy conductance that use satellite observations as a basis for predicting regional to continental-scale fluxes (Cleugh et al., 2007; Mu et al., 2007; Zhang et al., 2010). Leaf level stomatal conductance, for example, is constrained by minimum temperature and vapor pressure deficit (VPD), and then combined with satellite-derived LAI to calculate canopy level conductance for use in a modified PM equation to estimate canopy transpiration at a global scale (Cleugh et al., 2007; Mu et al., 2007). A semi-empirical algorithm also has been developed to estimate ET by relating aerodynamic conductance with wind speed and relating surface conductance with vegetation index and relative humidity deficit (Wang et al., 2010).

The Priestley–Taylor (PT) equation is a modified and simplified PM method without complex parameterizations of aerodynamic and surface resistance (Priestley & Taylor, 1972) and has been shown to have both a theoretical basis and experimental support (Eichinger et al., 1996). Sumner and Jacobs (2005) show that the PT method, where α is parameterized as a function of green LAI and solar radiation, provides the highest correlation with ET measurements, whereas the PM method, in which the bulk surface conductance is a function of net radiation (R_{net}) and vapor-pressure deficit, is slightly less effective in pastures. A contextual interpretation of the triangle-space of remotely sensed NDVI and LST over Southern Great Plains is used to estimate the PT coefficient and evapotranspiration without any ground-based data (Jiang & Islam, 2001). This approach assumes differences in surface temperature are caused primarily by evaporation from a given scenario of R_{net}. Alternatively, Fisher et al. (2008) show that it is possible to scale potential LE to actual LE based on ecophysiological constraints (LAI, green fraction of the canopy, plant moisture, and plant temperature) without using any ground data.

Here we developed a PT-based semi-empirical approach based on AmeriFlux eddy covariance measurements for estimating ET at regional to continental scales using MODIS satellite observations. We used satellite observations in two ways: (1) we used MODIS albedo and land surface temperature (LST) along with meteorological data to estimate R_{net}, and (2) we used MODIS LAI to dynamically adjust the PT coefficient (α) during each monthly time step. A unique aspect of our approach is the calculation of calibrated satellite estimates of regional R_{net} and ground heat flux at a high spatial resolution. We found that the satellite-based monthly R_{net} estimates agreed reasonably well with field measurements. Key questions in the context of PT α optimization include: (1) What biophysical and environmental variables control α on seasonal time scales? and (2) What is the best way to parameterize α across different ecosystem types. We optimized α as a function of LAI and soil moisture for individual sites and for major biomes using AmeriFlux measurements from 27 sites distributed across North America (Baldocchi et al., 2001). We then integrated this ET algorithm into the soil moisture module of the Carnegie–Ames–Stanford-Approach (CASA) biogeochemical model (Potter et al., 1993). Our results showed improvements for both ET and soil moisture estimates. The analysis of regional ET estimates over the conterminous United States (CONUS) indicated the shift of constraints for ET from water to available energy with increasing precipitation. Finally we estimated ET and runoff for continental river basins, and compared the results with previous estimates derived from the GRACE satellite and river discharge.

2. Data and methods

Our algorithm is based on the PT semi-empirical approach (Priestley & Taylor, 1972):

$$\lambda E = \alpha \frac{\Delta(T_a)}{\Delta(T_a) + \gamma(T_a)} (R_{net} - G) \tag{1}$$

where λE is the latent heat flux in W m^{-2}, α is the PT coefficient, $\Delta(T_a)$ is the slope of the relationship between saturation vapor pressure and air temperature, and $\gamma(T_a)$ is the psychrometric constant. Both Δ and γ are a function of air temperature (T_a). R_{net} and G are net radiation and ground heat flux in W m^{-2}, which were estimated using satellite data as described in Sections 2.1 and 2.2 for regional ET estimates. We optimized the PT α coefficient based on tower observations as described in Section 2.3.

2.1. Regional net radiation estimate

Surface R_{net} is affected by both atmospheric and land surface properties, and estimation of surface R_{net} at a high spatial resolution is challenging. MODIS satellite observations provide high spatial resolution products of surface physical properties such as albedo and temperature/emissivity. These contribute to the heterogeneity in R_{net}. In contrast, the incoming solar radiation ($S^{\downarrow}$) and incoming longwave radiation ($L^{\downarrow}$) are mainly controlled by cloud cover and the profiles of aerosols, temperature, and water vapor, which tend to be less heterogeneous than surface properties. R_{net} and individual radiation components from the Clouds and the Earth's Radiant Energy System (CERES) at 1°×1° have high accuracy, but cannot resolve high resolution spatial heterogeneity caused by rapidly changing surface albedo and land surface temperature over short (~1 km) distances. Here we integrated the high resolution MODIS land surface products with relatively coarse resolution (but high quality) satellite products of $S^{\downarrow}$ and cloud fraction. This provided the highest possible spatial resolution of surface R_{net} for our regional estimates of ET (Sections 2.4 and 3.4):

$$R_{net} = S^{\downarrow}\cdot(1-albedo) + \varepsilon_s\cdot L^{\downarrow}(T_a, e, cloud) - L^{\uparrow}(T_s, \varepsilon_s). \tag{2}$$

We estimated net shortwave (SW) radiation (the first term on the right side of Eq. (2)) by combining satellite-derived surface $S^{\downarrow}$ and albedo. We used the monthly $S^{\downarrow}$ dataset for the CONUS from the Global Energy and Water Cycle Experiment (GEWEX) Americas Prediction Project Surface Radiation Budget (GAPP/SRB) data (http://www.meto.umd.edu/~srb/gcip/cgi-bin/main.cgi). This dataset uses a modified version of the GEWEX/Surface Radiation Budget (SRB) model (Pinker et al., 2002; Pinker et al., 2003) to generate $S^{\downarrow}$ from Geostationary Operational Environmental Satellites (GOES) observations at a 0.5°×0.5° spatial resolution from 1996 to present.

We derived monthly all sky shortwave albedo based on MODIS collection 5 surface Bidirectional Reflectance Distribution Function (BRDF)/albedo product (MOD43B1) during each 16-day interval at 1 km spatial resolution (Schaaf et al., 2002). The all sky albedo was calculated as a weighted sum of black-sky albedo and white sky albedo by the ratio of direct and diffuse incoming solar radiation over the total $S^{\downarrow}$. We calculated 3-hourly black-sky albedo from the MODIS BRDF parameters and used the 3-hourly monthly mean direct and diffuse radiation data from the GEWEX/SRB data set (Stackhouse et al., 2010) to derive 3-hourly and monthly mean all sky albedo (Jin et al., 2003a; Jin et al., 2003b).

Incoming longwave radiation ($L^{\downarrow}$) was estimated with the Stefan–Boltzmann law,

$$L^{\downarrow} = \varepsilon\cdot\sigma T_a^4 \approx \varepsilon_{clr}\cdot(1+\mu\cdot F^{\nu})\cdot\sigma T_a^4 \tag{3}$$

where σ is Stefan–Boltzmann constant and T_a is the absolute temperature (K) at the reference height (2 m). The all sky effective (or apparent) emissivity (ε) is mainly controlled by air temperature (T_a), atmospheric water vapor (e), and clouds. We adopted an empirical approach from Prata(1996) to estimate clear sky emissivity (ε_{clr}) for incoming longwave radiation,

$$\varepsilon_{clr} = 1-(1+\xi)\, exp\left\{-\left(1.2+3.0\xi\right)^{\frac{1}{2}}\right\} \tag{4}$$

where $\xi = 46.5\left(\frac{e_0}{T_a}\right)$, and e_0 is near-surface vapor pressure (hPa), and T_a is near-surface temperature (K). Under all sky conditions, the emissivity ε was estimated with cloud fraction (F) (Duarte et al., 2006):

$$\varepsilon = \varepsilon_{clr}\left(1+\mu\cdot F^{\nu}\right). \tag{5}$$

We used monthly 2 m air temperature (T_a) from the Oregon State University Parameter-elevation Regressions on Independent Slopes Model (PRISM) project at a 2.5 min (~4 km) resolution (Daly et al., 2008), near surface vapor pressure (e_0) from the NCEP reanalysis 2 project (http://www.cdc.noaa.gov) at approximately 210 km×210 km (Kalnay et al., 1996), and GAPP/SRB cloud fraction (F) derived from GOES observations at 0.5°×0.5° resolution (Pinker et al., 2003). We optimized parameters μ and ν based on monthly $L^{\downarrow}$ data from AmeriFlux observations (Section 2.3). These values were 0.317 and 3.250 using a non-linear least squares optimization procedure (LSQNONLIN) in MatLab (Coleman & Li, 1996).

The amount of energy emitted by land surface is dependent on surface temperature (T_s) and surface emissivity (ε_s). The outgoing longwave radiation ($L^{\uparrow}$) at surface was estimated with the Stefan–Boltzmann law using MODIS 8-day LST product at 1 km resolution from MODIS Terra (MOD11A2) and Aqua observations (MYD11A2) (Wan, 2008). Both MODIS Terra and Aqua make two daily observations, one during daytime, and the second at night. We estimated the daily mean surface temperature by fitting a two-phase sinusoidal model (Sun & Pinker, 2005) through the four MODIS Terra and Aqua temperatures. The monthly mean surface temperature was calculated as the average of daily means over each 8-day time period within each month. The emissivities over individual bands were converted to broadband emissivity using the conversion coefficients provided by Jin and Liang (2006). LST is retrieved only in clear-sky conditions, and is not contaminated by cloud-top temperature (Wan, 2008). Difference in $L^{\uparrow}$ and thus R_{net} during clear and cloudy periods introduces uncertainty and contributes to model biases and variability as shown in Section 3.2. Errors are probably relatively small in desert areas and increase in areas with higher levels of cloud cover.

We compared our estimated surface R_{net} with both the AmeriFlux observations (Section 2.3) and the monthly regional 1°×1° gridded Surface Radiation Budget average (SRBAVG-GEO) data product produced by the CERES project (Wielicki, 1996; Wielicki et al., 1998). It is available online at http://eosweb.larc.nasa.gov/PRODOCS/ceres/level3_srbavg_table.html. The CERES data products from Terra and Aqua represent a new generation of radiation budget data that use up to 11 instruments on 7 spacecraft to improve angular and temporal sampling (e.g., Wielicki et al., 1998).

2.2. Soil heat flux

We estimated total available energy as the balance between R_{net} and ground heat flux (G). G was derived using a modified empirical approach based on the algorithm developed by Su (2002):

$$G = c + \left(a\cdot f_{veg} + b\cdot f_{soil}\right)\cdot R_{net} \tag{6}$$

where parameters a and b represent the fractions of G over R_{net} for pure vegetation and soil, and parameter c is an offset. The fraction of vegetation (f_{veg}) and soil (f_{soil}) were estimated from the MODIS collection 5 LAI product (MOD15A2) at 1 km resolution and for 8-day intervals (Myneni et al., 2002), using the formula $e^{-0.4\cdot LAI}$ for f_{soil} (Su et al., 2001). We estimated a, b, and c using the AmeriFlux G and R_{net} observations (Section 2.3) at a monthly time scale with the LSQNONLIN optimization routine in MATLAB (Coleman & Li, 1996).

2.3. AmeriFlux data and PT α coefficient optimization

We chose to allow α to respond to both LAI and soil moisture because of large temporal offsets in the timing of peak R_{net} and peak LE in many shrubland and grassland sites as shown in Section 3.1. We formulated α as,

$$\alpha = a_1\cdot\left(1-e^{(-b_1\cdot LAI)}\right)\cdot\left(1-e^{(c_1-d_1\cdot VSM)}\right)\cdot f(T_a). \tag{7}$$

Where LAI is the leaf area index (typically varying from 0 to 6), VSM is volumetric soil moisture in $\frac{\text{cm}^3\text{water}}{\text{cm}^3\text{soil}}$. $f(T_a)$ is a temperature scalar, which was set to 0.05 when the near surface air temperature was below −5 °C and otherwise was set to 1. A set of four parameters (a_1, b_1, c_1, and d_1) required optimization.

We used AmeriFlux data and MODIS collection 5 LAI product (Myneni et al., 2002) in developing parameterizations of α. The AmeriFlux network provides continuous measurements of CO_2, water, energy, and meteorological variables every half hour across climate gradients and within multiple ecosystem types (Baldocchi et al., 2001). We focused on sites that had latent heat, R_{net}, and soil moisture observations from 2001 to 2006. A total of 27 sites met these criteria (Table 1). These sites included several plant functional types, and encompassed a broad range of temperature and soil moisture. Additionally, we used 7 sites that lacked soil moisture measurements

Table 1
Site characteristics for 27 AmeriFlux sites used for optimization and for 7 AmeriFlux sites used for validation.[a]

Site name	Veg.	Lat	Lon	R_{net}[b]	LAI[c]	VSM[b]	T_a[b]	LE[b]	α[b]	PI	Reference
Sites used for optimization											
Duke Hardwoods	DBF[d]	36.0	−79.1	94	4.1	0.35	15.2	54	0.94	R. Oren	Oishi et al. (2008)
Missouri Ozark	DBF[d]	38.7	−92.2	103	3.7	0.30	11.6	56	0.95	L. Gu	Gu et al. (2006)
Morgan Monroe	DBF[d]	39.3	−86.4	91	3.7	0.39	12.8	44	0.81	H. Schmid	Sims et al. (2008)
Bartlett	DBF[d]	44.1	−71.3	85	3.6	0.35	7.3	25	0.48	A. Richardson	Jenkins et al. (2007)
Willow Creek	DBF[d]	45.9	−90.1	78	2.6	0.31	5.9	27	0.65	P. Bolstad	Bolstad et al. (2004)
North Carolina LP	MF[d]	36.8	−76.7	111	5.2	0.32	14.7	86	1.26	J. Chen	Chen et al. (2004)
North Carolina CC	MF[d]	35.8	−76.7	98	4.4	0.42	10.5	71	1.30	J. Chen	Chen et al. (2004)
Sylvania Wilderness	MF[d]	46.2	−89.3	66	2.8	0.21	4.8	28	0.88	P. Bolstad	Desai et al. (2005)
Duke Forest Pine	ENF[d]	36.0	−79.1	98	4.1	0.29	14.8	58	0.97	G. Katul	Albertson et al. (2001)
Blodgett	ENF[d]	38.9	−120.6	113	4.1	0.23	11.4	55	0.86	A. Goldstein	Kurpius et al. (2003)
Metolius Intermediate	ENF[d]	44.5	−121.6	91	3.0	0.11	6.9	34	0.75	B. Law	Schwarz et al. (2004)
Wind River	ENF[d]	45.8	−122.0	96	3.1	0.30	9.7	38	0.72	K. Bible	Wharton et al. (2009)
Tonzi	Savanna	38.4	−121.0	101	1.8	0.21	16.6	31	0.47	D. Baldocchi	Baldocchi et al. (2004)
Toledo	Savanna	41.6	−83.8	88	3.6	0.19	10.3	50	1.02	J. Chen	Noormets et al. (2008)
Audubon	Grassland	31.6	−110.5	59	0.5	0.16	14.6	22	0.65	T. Meyers	
Kendall Grasslands	Grassland	31.7	−109.9	76	0.4	0.05	15.5	17	0.35	R. Scott	Scott et al. (2006)
Goodwin Creek	Grassland	34.3	−90.0	88	1.7	0.33	15.4	54	0.99	T. Meyers	Houborg et al. (2009)
ARM SGP Control	Grassland	35.5	−98.0	90	1.0	0.22	13.8	55	1.01	M. Torn	Sims and Bradford (2001)
ARM SGP Burn	Grassland	35.6	−98.0	84	1.0	0.25	14.1	50	0.93	M. Torn	Sims and Bradford (2001)
Walnut River	Grassland	37.5	−96.9	103	0.9	0.37	10.0	48	0.85	R. Coulter	Coulter et al. (2006)
Vaira	Grassland	38.4	−121.0	71	1.8	0.15	16.0	24	0.54	D. Baldocchi	Ryu et al. (2008)
Fermi Prairie	Grassland	41.8	−88.2	93	1.1	0.35	7.1	45	0.95	R. Matamala	Matamala et al. (2008)
Brookings	Grassland	44.3	−96.8	77	1.0	0.43	7.2	67	1.75	T. Meyers	Gilmanov et al. (2005)
Fort Peck	Grassland	48.3	−105.1	52	0.4	0.25	6.0	27	1.19	T. Meyers	
ARM SGP Main	Cropland	36.6	−97.5	80	0.8	0.25	15.4	37	0.70	M. Torn	Sims and Bradford (2001)
Bondville	Cropland	40.0	−88.3	82	0.9	0.30	11.6	49	1.06	T. Meyers	Hollinger et al. (2005)
Fermi Agriculture	Cropland	41.9	−88.2	80	1.1	0.32	7.5	48	1.17	R. Matamala	Matamala et al. (2008)
Sites used for validation											
Harvard Forest	DBF[d]	42.5	−72.2	71	4.2	–	8.1	31	0.95	J. Munger	Urbanski et al. (2007)
Little Prospect Hill	DBF[d]	42.5	−72.2	–	3.6	–	5.3	44	–	J. Hadley	Hadley et al. (2008)
Howland Forest Main	MF[d]	45.2	−68.7	72	5.2	–	6.5	26	0.73	D. Hollinger	Hollinger et al. (2004)
Park Falls	MF[d]	45.9	−90.3	62	3.3	–	5.3	34	1.05	K. Davis	Davis et al. (2003)
Donaldson	ENF[d]	29.8	−82.2	107	2.5	–	20.2	74	0.96	T. Martin	Powell et al. (2005)
Mize	ENF[d]	29.8	−82.2	119	4.3	–	19.8	75	0.86	T. Martin	Powell et al. (2005)
Lost Creek	Shrubland	46.1	−90.0	63	3.1	–	4.7	29	0.97	A. Desai	Davis et al. (2003)

[a] Physical properties are annual means from AmeriFlux Level 2 data during 2001~2006. More site information can be found at (http://public.ornl.gov/AmeriFlux).

[b] Volumetric soil moisture (VSM), air temperature (T_a) in degrees Celsius, and latent heat (LE) and net radiation (R_{net}) in units of W m^{-2} from field measurements. Also shown are Priestley–Taylor α coefficients derived from Eq. (1).

[c] Leaf area index from MODIS.

[d] DBF: deciduous broadleaf forest; ENF: evergreen needleleaf forest; MF: mixed forest.

for the validation of our ET algorithm. We obtained level 2 half hourly data from the Oak Ridge National Lab (ORNL) Carbon Dioxide Information Analysis Center (CDIAC) ftp server (ftp://cdiac.ornl.gov/pub/AmeriFlux/data/Level2/). Data from individual sites were reviewed and checked to generate a consistent level 2 data set in a standardized format. We then averaged the half hourly data to daily, 8-day, and monthly time intervals. The α values at each individual site were derived through inversion of the Eq. (1) at all these time scales.

We performed three sets of optimizations for the parameters in Eq. (7): (1) for each site, (2) for each plant functional type, and (3) with one set of parameters across all biomes, respectively, at a monthly time step. The optimization involved minimizing the difference between observed α (derived by inverting Eq. (1) using tower observations of R_{net}, G, T_a, and LE) and the predicted α using MODIS LAI and tower-measured soil moisture and temperature as predictors. We performed the minimization for each individual site using monthly data, which is hereafter called the site-based optimization. For regional or global applications, it is more useful to obtain the parameterization of Eq. (7) over different plant functional types, or to obtain a more general global parameterization if errors are within an acceptable range. We thus grouped the AmeriFlux data into 4 biome types: 1. broadleaf forests; 2. needleleaf and mixed forests; 3. grasslands, shrublands and savannas; and 4. agriculture, and performed an optimization for each type, which we hereafter refer to as the plant functional type-based (PFT-based) optimization. We performed the optimization for 4 broad PFTs instead of each individual land cover types because of the limited number of available sites for specific land cover types such as savanna and shrublands. The PFT-based optimization is the average representation of all the land cover types within each PFT. For agriculture, we did another optimization where we set the soil moisture scalar in Eq. (7) to 1 over irrigated croplands (thus removing water stress constraints in areas with ample water supply). A global optimization was also done using all the AmeriFlux data in which we solved for a single set of coefficients in Eq. (7). For comparison, we also performed an optimization of a constant α for each site, hereafter called time-invariant optimization.

2.4. Implementation in the CASA biogeochemical model over CONUS

The CASA biogeochemical model simulates soil moisture using a simple bucket hydrology model (Potter et al., 1993). ET is a major loss pathway for water, and the soil water content at the current time step is calculated from the previous soil water content plus current precipitation minus actual ET. The excess of estimated soil water content over field capacity is output as drainage. The ET estimate in the original version of CASA was based primarily on the Thornthwaite potential ET (PET) approach using air temperature, latitude, and an annual heat index (Thornthwaite, 1948).

We modified the ET estimate in CASA using our PT algorithm with a PFT-based optimization as described in Section 2.3. Soil moisture at previous time step from CASA was used to estimate α using Eq. (7)

together with MODIS LAI. We set the extractable water (the previous soil water content plus current precipitation minus wilting point) as the upper bound of ET at the current time step. We also modified field capacity based on % sand, % clay, and % silt (Bonan, 1996; Yang et al., 1998) to better represent spatial variability in soil properties. Monthly maps of R_{net} and G were derived following the approach described in Sections 2.1 and 2.2, using information from MODIS observations. We performed a PFT-based optimization for our regional application using our regional maps of R_{net} and ground heat flux instead of the tower measured quantities using the same method described in Section 2.3. The regional ET and soil moisture were then derived over CONUS at 1 km spatial resolution at a monthly time scale during 2006 to 2008. MODIS IGBP land cover types (Friedl et al., 2002) were aggregated to 4 plant functional types. For the cropland identified by MODIS, we used the 2002 1 km irrigated land map <http://earlywarning.usgs.gov/usewem/> (Pervez & Brown, 2010) to identify irrigated cropland— in these areas we used optimization parameters that did not include a soil moisture constraint.

We used monthly temperature and precipitation data at a 2.5 min (~4 km) resolution from PRISM (Daly et al., 2008) as meteorological

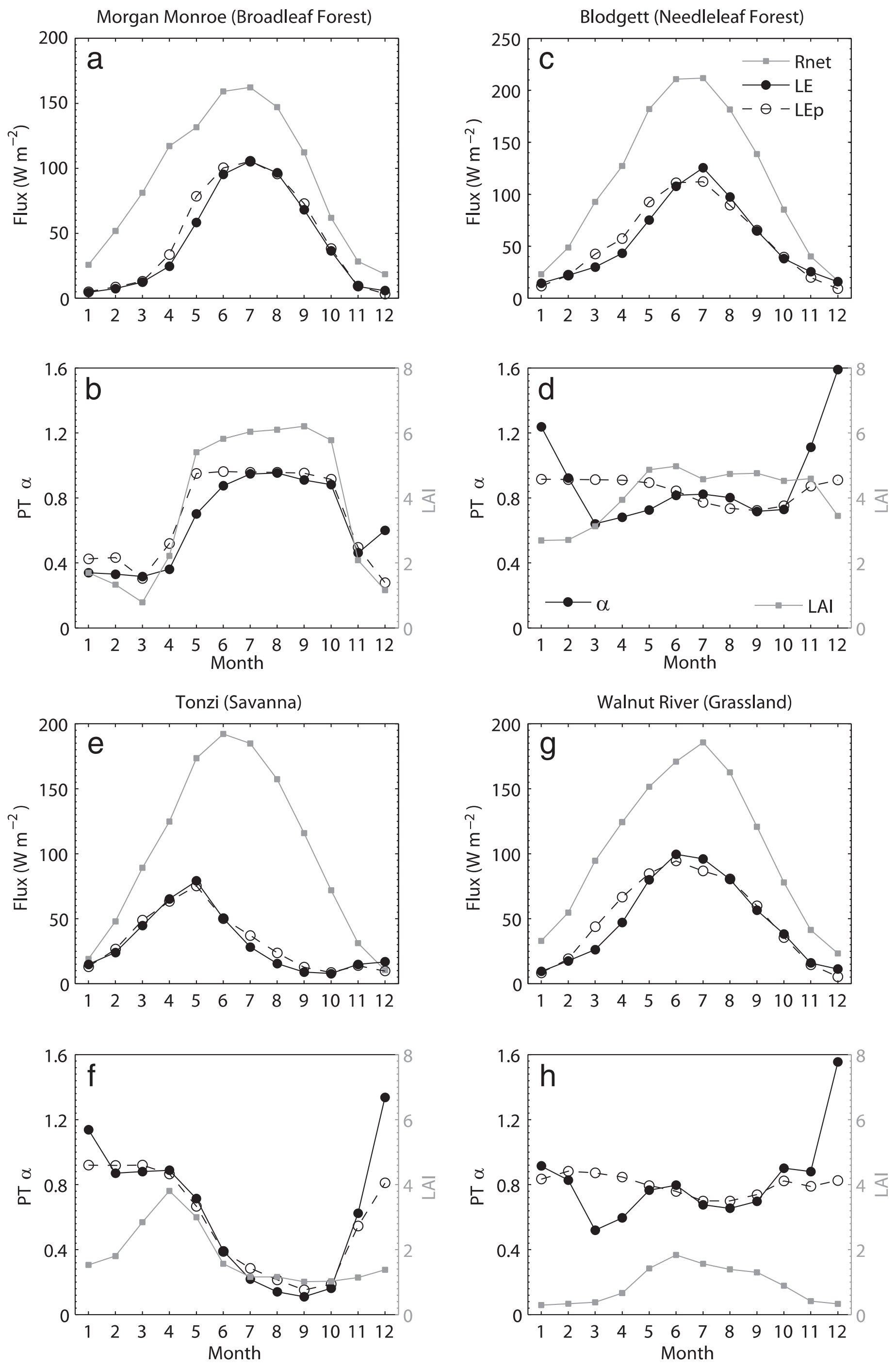

Fig. 1. Net radiation (R_{net}), latent heat (LE), leaf area index (LAI), and the Priestley–Taylor α coefficient for (a, b) Morgan Monroe, (c, d) Blodgett, (e, f) Tonzi, and (g, h) Walnut River sites. All quantities are monthly means averaged over the multi-year time period of each observation station. The open circles and dashed lines show the predicted latent heat (LE_p) (a,c,e,g) and PT α coefficients (b,d,f,h) from site based optimization using tower measurements.

inputs for CASA. Soil water content was initialized with zero value and the hydrology model was spun up for 5 years using the 3 year average of all input variables to reach steady state, and then the interannual run was performed using the interannually varying input variables to estimate ET and then soil moisture at each monthly time step. ET estimates were compared with the original version CASA ET and official MODIS ET (MOD16) product (Mu et al., 2007) over all AmeriFlux sites, and validated with the tower measurements at 7 sites that did not have soil moisture measurements. We also compared basin scale ET and runoff derived from CASA ET and the PRISM precipitation dataset with those from MOD16 ET and annual river discharge data.

2.5. Data preprocessing

MODIS albedo, land surface temperature and LAI data were aggregated to a monthly time scale for our regional ET estimates for CONUS. A linear regression method was applied to detect and remove poor quality data. We then linearly interpolated gaps in the LAI record. All the input datasets were preprocessed to a 1 km resolution at a common Albers equal area projection.

2.6. Model performance

For each optimization, we summarized the correlation and *p* values of the predicted α and those derived from tower data, as well as the correlation, root mean square error (RMSE), mean bias, and Taylor score of the predicted latent heat flux. We also used Taylor diagrams (Taylor, 2001) to summarize the performance of each optimization in predicting LE to visualize and quantify how closely the modeled LE resembled the observed LE.

3. Results

3.1. Controlling factors for latent heat flux

3.1.1. Seasonal patterns of latent heat flux

Fig. 1 shows multi-year mean monthly R_{net} and latent heat from observations at 4 tower sites, along with LAI from MODIS and α estimated directly from the flux tower observations using Eq. (1). R_{net} at all sites reached a maximum in June or July corresponding to the maximum incoming solar radiation. Latent heat followed a similar seasonal cycle in broadleaf forests (Fig. 1a, Morgan Monroe), where there was ample water for evapotranspiration. LAI and soil moisture had a seasonal pattern in this deciduous forest that was similar to R_{net}. At the Blodgett needleleaf forest site, the volumetric soil moisture started to decrease from April and reached a minimum in September (Fig. S1b), whereas LAI increased from January through May and remained high until November (Fig. 1d). As a consequence of the changes in these two opposing drivers, ET peaked in July in phase with R_{net} (Fig. 1c). In contrast, at many grassland sites, including the Tonzi savanna site in California (Fig. 1e, f) and the Walnut River grassland site in Kansas (Fig. 1g, h), LE reached a maximum prior to R_{net} as a consequence of the moisture limitation on leaf area and conductance.

The seasonal cycle of latent heat was very different from that of R_{net} at the Tonzi savanna site, where latent heat peaked earlier than R_{net}. The soil was wet from January to March during the winter rainy season (Fig. S1c), and R_{net} was much lower (by a factor of two) in winter than in summer. The latent heat increased gradually in spring with increases in R_{net} and leaf area. In April, LAI reached a maximum of 3.8 and then declined to 40% of this maximum by June. The maximum latent heat in May reflected a tradeoff between decreasing leaf area index (and soil moisture) and increasing R_{net}. This is typical for a Mediterranean climate and indicated that soil water content and leaf area index regulated the seasonal trajectory of ET in addition to R_{net} or available energy.

Walnut River is a mix of C3 and C4 tallgrass prairie, with cattle grazing (Coulter et al., 2006). The maximum of R_{net} occurred in July (186 $\mathrm{W\,m^{-2}}$) and LAI peaked in June (1.8). Both R_{net} and LAI controlled the seasonality of latent heat flux, and the maximum latent heat flux (99 $\mathrm{W\,m^{-2}}$) occurred in June. Soil moisture showed an opposite seasonality from LAI, with monthly mean volumetric soil moisture ranging from 52% in February to 24% in August. Soil moisture also played an important role in regulating LE, e.g., α was higher in June than in August due to higher soil moisture.

3.1.2. Controls on latent heat flux

Table 2 summarizes the correlation of monthly latent heat flux with monthly R_{net}, available energy, LAI, and soil moisture at a monthly time scale. Variation in R_{net} or available energy explained 65% to 80% of the variance in monthly latent heat at 26 of 34 sites (including the 7 validation sites). The correlation in all forest sites was higher than 0.80. Available energy was not always a good predictor of LE in savanna and shrubland ecosystems. The correlation coefficients ranged from 0.50 at Tonzi savanna, 0.61 at the Audubon open shrubland site in Arizona, and 0.82 at the Toledo oak woodlands/savanna/prairie complexes in Ohio. Correlations were low at some of the grassland sites, including, for example, the Vaira tower in California (0.16) and the Kendall tower in Arizona (0.48). These sites had mean annual soil moisture levels that were less than 15%.

As expected, leaf area index was highly correlated with latent heat fluxes for most forest and cropland sites. LAI also accounted for much of the variance of LE in biomes where R_{net} was not a dominant controller (e.g., grasslands and savannas). For example the correlation

Table 2
Pearson correlation between monthly latent heat (LE) and net radiation (R_{net}), available energy (AE), leaf area index (LAI), and volumetric soil water content (VSM).

Site name	R_{net}	AE	LAI	VSM
Duke Forest Hardwood	0.90	0.90	0.88	−0.55
Missouri Ozark	0.89	0.90	0.85	−0.77
Morgan Monroe	0.88	0.89	0.85	−0.43
Bartlett	0.90	0.91	0.81	*−0.33
Willow Creek	0.83	0.83	0.89	*−0.07
North Carolina LP	0.90	0.89	0.83	−0.56
North Carolina CC	0.86	0.87	0.92	−0.48
Sylvania Wilderness	0.82	0.82	0.92	*−0.24
Duke Forest Pine	0.91	0.91	0.86	−0.51
Blodgett	0.92	0.92	0.52	−0.65
Metolius Intermediate Pine	0.85	0.86	0.48	*−0.12
Wind River	0.91	0.90	0.60	−0.55
Tonzi	0.50	0.51	0.77	0.27
Toledo	0.82	0.81	0.91	−0.64
Audubon	0.61	0.76	0.71	0.42
Kendall Grasslands	0.48	0.52	0.64	0.80
Goodwin Creek	0.88	0.88	0.75	*−0.22
ARM SGP Control	0.93	0.94	0.86	*0.30
ARM SGP Burn	0.92	0.93	0.85	0.31
Walnut River	0.96	0.95	0.96	−0.52
Vaira	*0.16	*0.21	0.84	0.53
Fermi Prairie	0.92	0.92	0.82	−0.50
Brookings	0.90	0.92	0.73	0.52
Fort Peck	0.70	0.77	0.73	0.55
ARM SGP Main	0.67	0.64	0.57	*0.20
Bondville	0.83	0.81	0.71	*−0.05
Fermi Agriculture	0.87	0.87	0.61	−0.46
Harvard Forest	0.81	0.78	0.74	–
Little Prospect Hill	0.87	0.88	0.89	–
Howland Forest Main	0.82	0.82	0.61	–
Park Falls	*0.09	*0.29	0.88	–
Donaldson	0.64	0.63	*−0.13	–
Mize	0.85	0.82	0.58	–
Lost Creek	0.89	0.87	0.88	–

Statistics are derived from monthly AmeriFlux data and MODIS LAI from 2001 to 2006. The correlations that are not significant ($p>0.05$) are denoted with *.

coefficient of LE vs. LAI was 0.77 at the Tonzi savanna and 0.84 at the Vaira grassland. Soil moisture alone was not significantly correlated with LE at many sites, with a few exceptions. Figs. 1 and 2 show that α inverted directly from the observations was correlated with LAI and/or soil moisture at several sites.

3.2. Available energy

The seasonal cycle of remote sensing-derived R_{net} agreed reasonably well with field-based R_{net} measurements at representative towers (Fig. 3). These estimates were constructed using GOES $S^{\downarrow}$

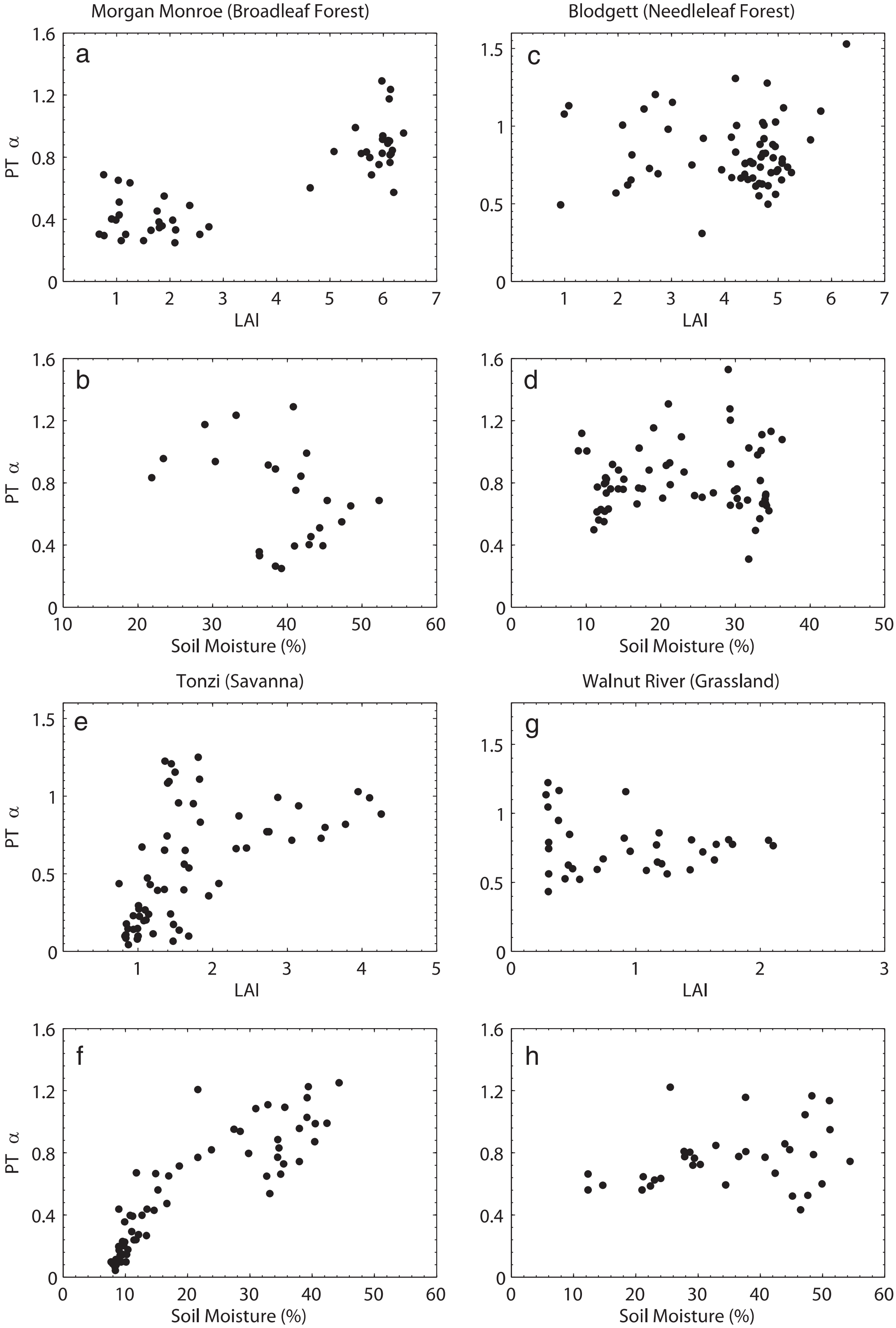

Fig. 2. Monthly Priestley–Taylor α coefficients vs. LAI and soil moisture at the site level for (a, b) Morgan Monroe, (c, d) Blodgett, (e, f) Tonzi, and (g, h) Walnut River sites.

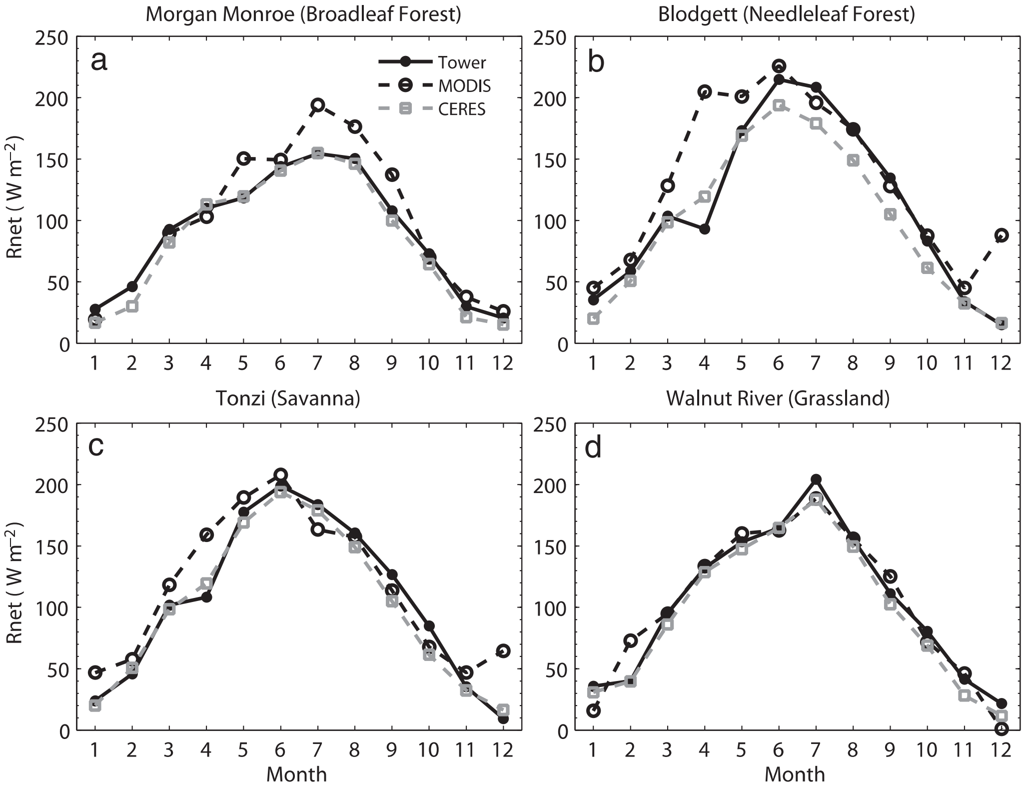

Fig. 3. Seasonal net radiation (24 hour means) from the tower measurements, MODIS, and CERES satellite observations during 2003 for (a) Morgan Monroe, (b) Blodgett, (c) Tonzi, and (d) Walnut River. MODIS net radiation was estimated using GOES incoming solar and MODIS albedo for the the shortwave radiation and MODIS LST/emissivity, GOES cloud fraction, PRISM near surface temperature and tower near surface vapor pressure for the longwave radiation.

and MODIS albedo for shortwave radiation, MODIS land surface temperature and emissivity for $L^{\uparrow}$, and PRISM near surface temperature and GOES cloud fractions and tower water vapor pressure for $L^{\downarrow}$. Over all sites, the estimated monthly R_{net} also agreed well with the tower measurements, with a correlation coefficient of 0.84, though there was a bias of 22 W m^{-2} (Fig. 4a and Table 3). The coarser resolution CERES monthly surface R_{net} also agreed well with the field measurements (Fig. 4a). The CERES R_{net} was systematically higher than the tower measurements (Fig. 4a), though the bias (8 W m^{-2}) was less than that of the MODIS-based estimate.

Monthly shortwave (SW) net radiation from both MODIS and CERES were correlated with the tower measurements, with correlation coefficients around 0.75 and RMSEs around 32 W m^{-2}, and a high bias (Table 3). The two satellite-derived net SW data sets agreed better with each other ($r = 0.94$, RMSE = 17.9 W m^{-2}) than with the tower measurements, though MODIS had a high bias of 9 W m^{-2} compared with CERES. A further analysis of the radiation components showed that the GOES $S^{\downarrow}$, which we used to derive MODIS SW radiation, had a high bias of 11 W m^{-2} compared with CERES $S^{\downarrow}$, although they were highly correlated ($r = 0.93$). We thus adjusted GOES $S^{\downarrow}$ based on the regression of CERES $S^{\downarrow}$ against GOES $S^{\downarrow}$ ($S^{\downarrow}_{adj} = -14.36 + 1.02\ S^{\downarrow}$).

The near surface vapor pressure had a large impact on $L^{\downarrow}$ and thus R_{net} across all sites. $L^{\downarrow}$ estimated with tower measured 2 m air temperature and the near surface vapor pressure derived from tower humidity was highly correlated with tower measured $L^{\downarrow}$ ($r = 0.83$, RMSE = 23 W m^{-2} and bias = 12 W m^{-2}). For regional estimates, we used the PRISM air temperature and near surface vapor pressure from NCEP reanalysis, which introduced additional errors. The correlation coefficient was reduced to 0.51 and bias increased to 15 W m^{-2} (Table 3). Overall, the correlation between MODIS and CERES $L^{\downarrow}$ was significant and the bias among them was small.

Outgoing longwave radiation $L^{\uparrow}$ estimated with MODIS land surface temperature and emissivity closely matched the field measurements ($r = 0.80$, RMSE = 24 W m^{-2}, bias = -3 W m^{-2}). When compared with the tower measurements, CERES $L^{\uparrow}$ had similar statistics ($r = 0.77$, RMSE = 26 W m^{-2}, bias = 0.3 W m^{-2}). Compared with CERES, the MODIS $L^{\uparrow}$ had a low bias of -7 W m^{-2} with a correlation coefficient of 0.92. Based on this and the limitation that MODIS LST was retrieved only under clear sky conditions, we applied an adjustment to MODIS $L^{\uparrow}$ with an intercept of 33.62 and a slope of 0.93. We then calculated the R_{net} with the adjusted $S^{\downarrow}$ and the adjusted $L^{\downarrow}$ for the regional estimates presented below in Section 3.4. The bias from the adjusted MODIS R_{net} was reduced to -0.7 W m^{-2} and correlation was increased to 0.76 compared with CERES R_{net} (Fig. 4b). The bias was reduced from 25 to 6 W m^{-2}, and RMSE was reduced from 44 to 31 W m^{-2} as compared with R_{net} from the tower measurements.

From our optimization of ground heat fluxes using Eq. (6), we found that monthly G was approximately equal to 10% of R_{net} in low LAI ecosystems, and 5% in forest ecosystems at monthly time step. These estimates are probably adequate for use in temperate ecosystems that undergo large seasonal changes in temperature and solar radiation, but may be inappropriate for use in other biomes. The semi-empirical method captured the seasonal cycle of ground heat flux. There were some discrepancies between our model estimates of ground heat flux and field measurements. However, the ground heat flux is only a small fraction of R_{net} at a monthly time scale, and this probably did not introduce substantial errors in our estimates of available energy.

3.3. Optimization of the PT α coefficient

3.3.1. Site-based optimization

Fig. 1 shows that the model-predicted α had a similar seasonal pattern to the α obtained from a direct inversion of the monthly observations. Savanna and deciduous broadleaf forest sites experienced

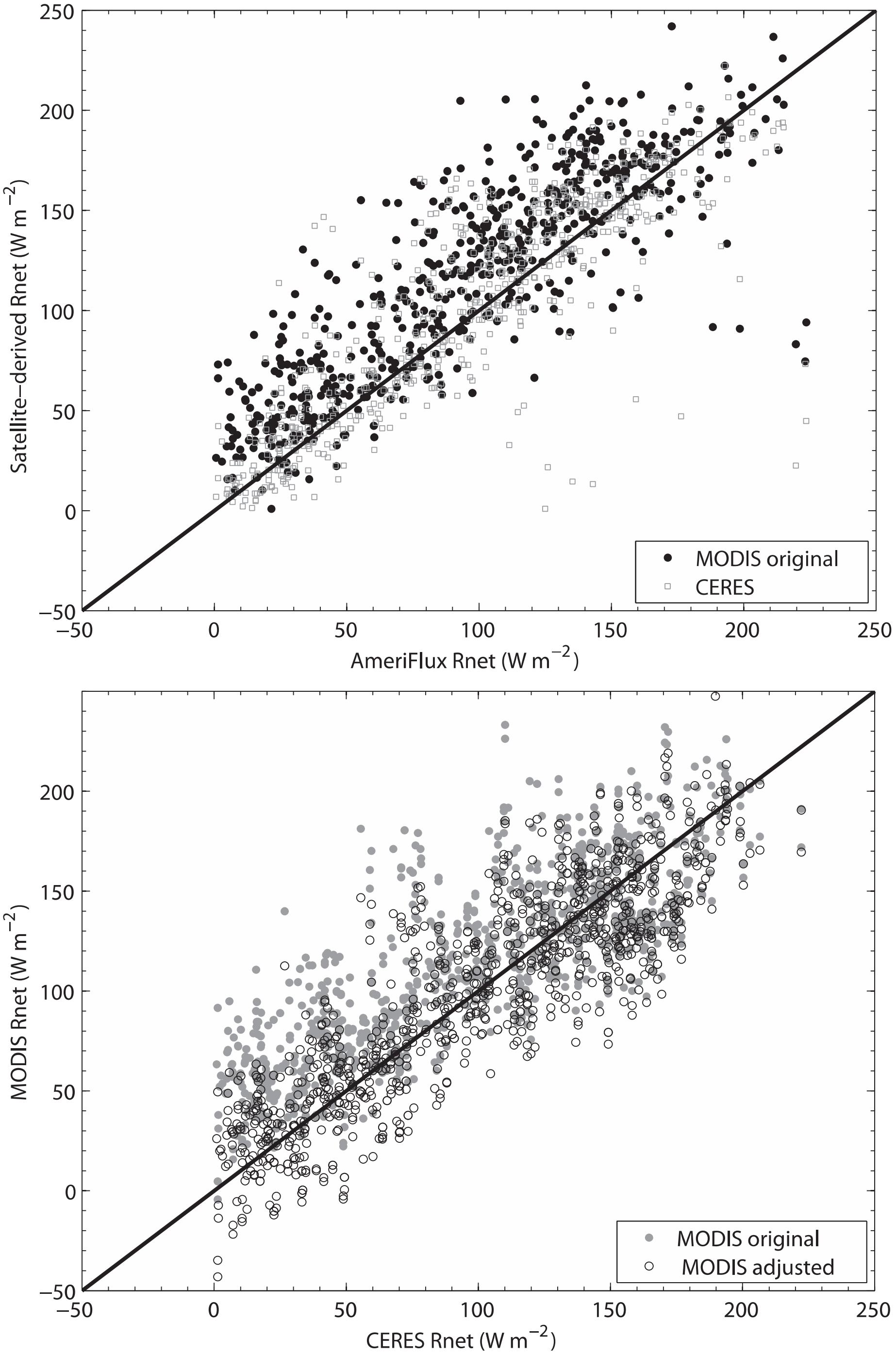

Fig. 4. Monthly net radiation from MODIS and CERES satellite observations, compared with the field observations over AmeriFlux tower sites during 2003 and 2004. MODIS net radiation was estimated with tower near surface vapor pressure for incoming longwave radiation in top panel, and was estimated with NCEP reanalysis vapor pressure and adjusted based on CERES incoming and outgoing longwave radiation in the bottom panel.

the largest change of α over the year, while the amplitude of α at the Blodgett needleleaf forest and Walnut River grassland sites was much smaller. Similarly, predicted latent heat fluxes agreed reasonably well with observations at all 4 sites. Fig. 5 shows that for the site-based optimization, model estimates of α and LE reproduced much of the observed variability at a monthly time scale over all 27 AmeriFlux sites. The agreements between the predictions and the observations were better for the annual mean. Table 4 showed that the RMSE of predicted LE from site-based optimization ranges from 5 $\mathrm{W\,m^{-2}}$ at the Kendall Grassland site (26 monthly observations) to 22 $\mathrm{W\,m^{-2}}$ at the Fermi agriculture site (15 monthly observations). The predicted LE from the site-based α optimization was more strongly correlated with the observed LE than predictions with time-invariant α, especially over savannas and grasslands (Table 4). Compared with the time-invariant α, the average RMSE of predicted monthly LE decreased from 15 $\mathrm{W\,m^{-2}}$ to 12 $\mathrm{W\,m^{-2}}$, and the Taylor score increased from 0.70 to 0.84 across all sites.

3.3.2. Plant functional type-based optimization

The Taylor scores for predicted LE decreased slightly from 0.84 to 0.79 when we performed the optimization for four different biome types, and the RMSE increased on average from 12 $\mathrm{W\,m^{-2}}$ to

Table 3
Comparison of radiation components between tower measurements and radiation estimates derived from MODIS and CERES satellite observations.

	SW_{in}	SW_{out}	SW_{net}	LW_{in}	LW_{in0}	LW_{out}	LW_{net}	R_{net}	R_{net0}	R_{net_adj}
					MODIS vs. Tower					
RMSE	37.6	16.4	34.3	37.3	23.3	24.3	31.4	44.4	30.8	30.5
Bias	3.0	−5.7	7.4	15.1	12.4	−2.7	17.8	25.3	22.1	6.2
Corr	0.76	0.54	0.75	0.51	0.83	0.80	0.42	0.57	0.84	0.56
					CERES vs. Tower					
RMSE	36.1	20.3	32.0	31.9		25.6	22.0	36.2		
Bias	−3.7	−7.6	3.8	6.0		0.3	5.7	8.1		
Corr	0.79	0.48	0.78	0.61		0.77	0.65	0.64		
					MODIS vs. CERES					
RMSE	22.1	12.6	17.9	27.0	29.3	16.1	26.3	35.5	29.8	27.1
Bias	10.8	2.1	8.7	0.3	−4.8	−7.3	7.6	16.3	11.2	−0.7
Corr	0.93	0.37	0.94	0.68	0.55	0.92	0.11	0.67	0.62	0.76

SW_{out} was calculated with MODIS albedo and GOES incoming solar radiation.

LW_{in0}: Incoming longwave radiation using tower vapor pressure instead of NCEP reanalysis near vapor pressure.

R_{net0}: Total net radiation with LW_{in0}.

R_{net_adj}: Adjusted MODIS based net radiation used for our regional ET estimate. Specifically the biases in incoming shortwave and outgoing longwave radiation were adjusted based on CERES radiation components.

17 W m^{-2} (Table 4). The biggest RMSE increases occurred in grasslands, for example, from 5 to 16 W m^{-2} at the Kendall grassland site. The performance of the PFT-based prediction was still better than the predictions by time-invariant site-specific α, as shown by the higher correlation coefficients and Taylor scores. Table 5 shows the parameters derived from the optimization of Eq. (7) for the 4 different plant functional types. Croplands had the largest maximum α of around 1.2, followed by grassland/savannas/shrubland, while forests had lower α in general (Fig. S2). LAI affected ET in all biome types and α increased as a function of LAI when LAI was less than 1 for non-forest biomes. ET was very sensitive to soil moisture when VSM is less than 0.25 for all biomes, and ET for forests was not dependent on moisture at higher levels of VSM.

3.3.3. Global optimization

Many sites showed a small reduction in model performance or no significant change for the global optimization relative to the PFT optimization (Table 4). Several sites showed moderate reductions including the Metolius Intermediate Pine and the Tonzi savanna sites. On average, the Taylor scores decreased from 0.79 to 0.75. LAI did not influence α strongly except when/where LAI was much less than one.

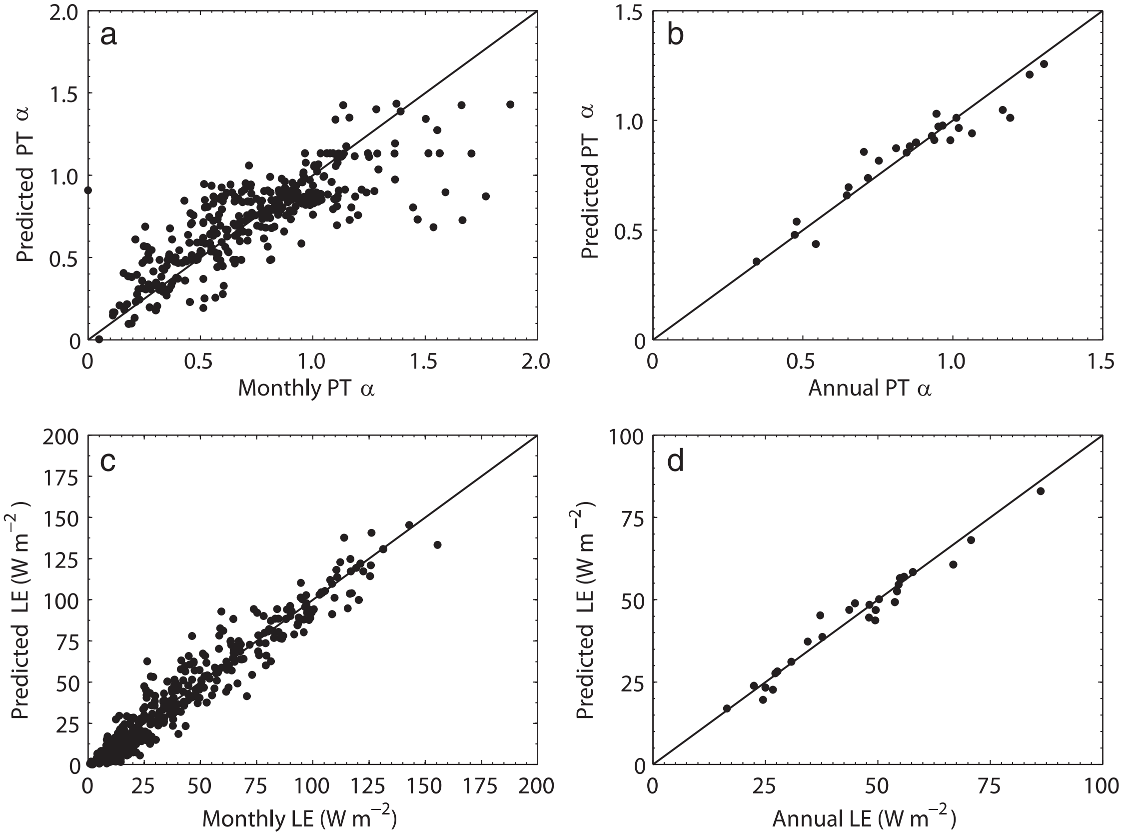

Fig. 5. Scatterplot of predicted Priestley–Taylor α coefficients (a, b) and LE (c, d) from the site-based optimization vs. tower measurements over 27 AmeriFlux sites from 2001 to 2006. (a) and (c) are for multi-year monthly values while (b) and (d) are for multi-year annual means.

Table 4
Statistics of comparison between monthly latent heat and those predicted from four sets of Priestley–Taylor optimizations.[a]

Site name	Code	N_{obs}	RMSE[a]				Correlation				Bias[a]				Taylor score			
			F[b]	Site[c]	PFT[c]	G[c]	F[b]	Site[c]	PFT[c]	G[c]	F[b]	Site[c]	PFT[c]	G[c]	F[b]	Site[c]	PFT[c]	G[c]
Duke Hardwoods	a	31	11	11	9	13	0.95	0.95	0.97	0.94	1.0	1.4	−3.4	1.6	0.89	0.89	0.95	0.87
Missouri Ozark	b	22	20	19	16	18	0.87	0.88	0.93	0.91	0.3	3.2	−2.5	3.5	0.75	0.79	0.86	0.83
Morgan Monroe	c	24	18	13	14	18	0.92	0.96	0.95	0.91	3.9	2.7	−0.8	5.8	0.80	0.92	0.88	0.81
Bartlett	d	14	9	11	21	27	0.96	0.96	0.98	0.96	2.3	−2.7	18.1	24.6	0.89	0.83	0.89	0.86
Willow Creek	e	63	14	9	15	22	0.91	0.96	0.95	0.89	2.8	0.9	8.2	13.3	0.78	0.92	0.87	0.76
North Carolina LP	f	19	12	13	19	22	0.95	0.95	0.94	0.93	−1.0	2.6	−12.6	−16.9	0.91	0.91	0.88	0.87
North Carolina CC	g	19	13	13	14	17	0.93	0.94	0.93	0.92	0.2	2.9	−5.5	−9.4	0.86	0.88	0.87	0.84
Sylvania Wilderness	h	43	12	11	1	12	0.88	0.92	0.90	0.85	−0.7	3.7	1.8	1.2	0.75	0.84	0.81	0.74
Duke Forest Pine	i	51	13	10	10	10	0.92	0.95	0.96	0.96	−1.3	2.4	−0.4	−2.6	0.85	0.91	0.93	0.92
Blodgett	j	62	11	13	16	18	0.95	0.94	0.90	0.87	−0.5	3.0	1.5	−2.5	0.92	0.89	0.82	0.77
Metolius Intermediate	k	40	14	17	12	20	0.81	0.89	0.88	0.71	−2.7	−4.2	−7.7	−15.1	0.78	0.66	0.78	0.53
Wind River	l	38	10	12	30	27	0.92	0.90	0.90	0.91	−3.7	3.3	17.6	16.9	0.78	0.71	0.47	0.53
Tonzi	m	59	24	8	17	19	0.39	0.95	0.88	0.81	−2.6	2.3	12.0	12.0	0.19	0.92	0.77	0.67
Toledo	n	15	23	16	24	23	0.81	0.95	0.83	0.83	1.5	5.7	−7.3	−7.0	0.59	0.89	0.63	0.64
Audubon	o	14	13	5	10	10	0.75	0.96	0.85	0.85	0.7	−0.2	−0.3	0.1	0.45	0.92	0.74	0.73
Kendall Grasslands	p	26	16	5	16	15	0.38	0.96	0.90	0.90	−0.4	1.1	−13.1	−12.9	0.13	0.93	0.76	0.80
Goodwin Creek	q	41	10	11	22	18	0.94	0.94	0.86	0.86	−1.1	3.8	7.9	1.9	0.89	0.88	0.69	0.73
ARM SGP Control	r	12	17	7	16	17	0.83	0.98	0.96	0.96	0.8	0.2	−4.3	−6.4	0.63	0.96	0.86	0.84
ARM SGP Burn	s	16	17	9	15	15	0.92	0.97	0.95	0.95	2.6	−0.1	5.2	1.3	0.78	0.95	0.88	0.86
Walnut River	t	33	9	11	22	16	0.96	0.95	0.95	0.97	−0.4	2.5	14.7	10.0	0.93	0.90	0.84	0.90
Vaira	u	40	33	11	16	17	−0.14	0.93	0.78	0.72	−10.9	−1.2	−4.3	−4.2	0.01	0.85	0.56	0.50
Fermi Prairie	v	20	15	15	19	15	0.93	0.94	0.92	0.93	1.1	3.7	8.3	3.7	0.87	0.88	0.86	0.88
Brookings	w	13	18	17	28	34	0.90	0.93	0.92	0.92	−1.0	2.9	−19.6	−26.6	0.82	0.86	0.83	0.77
Fort Peck	x	12	10	9	18	20	0.74	0.73	0.83	0.83	−4.4	−2.7	−5.7	−7.8	0.52	0.54	0.66	0.62
ARM SGP Main	y	40	16	18	18	21	0.72	0.81	0.81	0.77	−3.2	6.5	6.4	9.9	0.55	0.61	0.61	0.54
Bondville	z	37	16	16	16	16	0.88	0.89	0.89	0.87	0.1	4.9	−6.3	−3.9	0.76	0.80	0.80	0.77
Fermi Agriculture	0	15	16	22	16	16	0.89	0.83	0.91	0.90	0.3	1.4	−2.6	−1.6	0.81	0.70	0.82	0.81
Average			15	12	17	18	0.81	0.92	0.90	0.88	−0.6	1.9	0.2	−0.4	0.70	0.84	0.79	0.75

[a] Root-mean-square-error (RMSE) and bias in W m^{-2} for latent heat flux, correlation, and Taylor score are derived from monthly AmeriFlux data from 2001 to 2006.
[b] F, one time-invariant Priestley–Talyor α value optimized for each site as shown in Eq. (1).
[c] Site, PFT, and G represent the optimizations of α for the site-based, plant functional type-based (PFT-based), and global-based optimizations, respectively. α was parameterized as a function of LAI and soil moisture as shown in Eq. (7).

Soil moisture influenced α significantly when VSM was below 0.25 on a global scale.

3.4. Improvement of ET estimates in the CASA biogeochemical model

3.4.1. Comparison of original and new CASA ET

The seasonal cycle of soil moisture estimated by CASA was similar to that from the field measurements at the Tonzi site from 2003 to 2005 (Fig. 6). The new version improved the prediction of soil moisture for all years. The model captured the seasonality of ET as measured in the field. The modeled LE was higher than the observations before May, due to a positive bias in R_{net} (Fig. 6d). The largest difference occurred during May and June, when there was a lag between the decrease of α predicted by the model. Overall, the ET predicted by the model agreed better than the ET simulated by the original version of CASA, as shown in the Taylor diagrams (Fig. 7a, b). Table S1 shows that the Taylor score increased from 0.68 to 0.73 on average compared with the original CASA over all 34 sites. Similarly, the mean bias was reduced from 6.6 mm mon^{-1} to 0.8 mm mon^{-1}. Most of these improvements in correlation and reduction in bias were a result of our use of our new estimates of LE derived from the remote sensing observations. Additional model simulations in which we used the new soil parameterizations (Bonan, 1996; Yang et al., 1998) and the original Thornwaite-based ET showed little or no overall improvement (data not shown).

Table 5
Coefficients derived from plant functional type-based (PFT), and global-based optimization (global) of Eq. (7).

Plant Function Type (PFT)	PFT-based optimization			
	a_1	b_1	c_1	d_1
Broadleaf forest	0.93	0.78	0.00	15.00
Needleleaf/mixed forest	1.08	1.07	0.00	8.36
Grassland, shrubland and savanna	1.17	5.50	0.30	7.70
Cropland	1.22	3.48	0.00	5.52
	Global optimization			
	a_1	b_1	c_1	d_1
All except cropland	0.94	5.53	0.00	10.26

We set the maximum of a_1 to be 2.0, and the maximum values for b_1, c_1, and d_1 to be 15.0.

3.4.2. Validation of new CASA ET over 7 sites

The 7 AmeriFlux sites not used for the optimization due to lack of soil moisture measurements were used to validate the modified CASA ET algorithm. The new CASA ET captured the seasonality of ET, i.e., it captured the decrease of ET from May to June at Mize for each year, better than the old version (Fig. S3). The RMSE and Taylor score were 25 mm mon^{-1} and 0.7, respectively, averaged over these validation sites (Table S1). The performance of our algorithm was also better than the MODIS (MOD16) ET product (Taylor score of 0.64) (Table S1, Fig. 7c and Fig. S3).

3.4.3. Validation at large spatial scales

We applied the approach presented in Section 2.4 to CONUS to estimate ET from 2006 to 2008 at 1 km resolution. Our basin scale monthly ET estimates averaged over the Mississippi River basin (with a total drainage area of 3.21 million km^2) from 2006 to 2008 showed a strong seasonal pattern, ranging from 0 in January to 3.1 mm/day in June/July (Fig. 8a). Both the seasonality and magnitude were similar to the basin scale ET results obtained by Rodell et al. (2004). In Rodell et al.

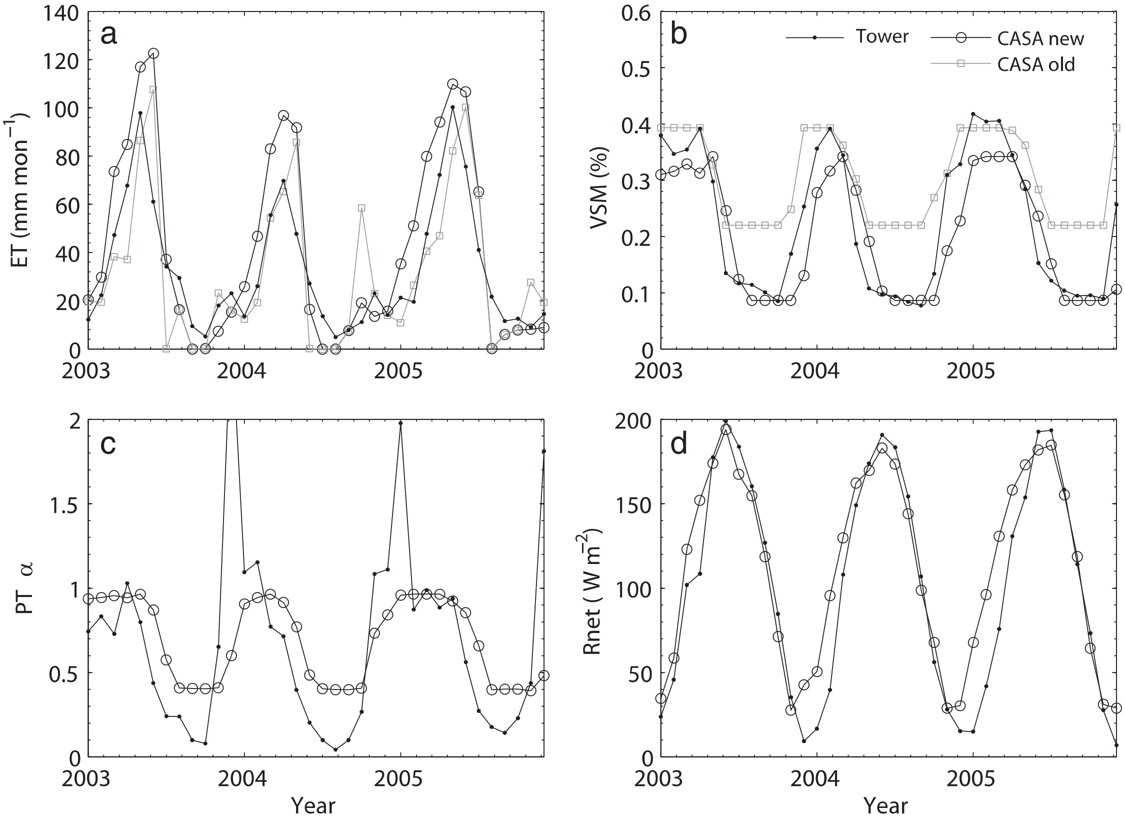

Fig. 6. Time series of (a) monthly evapotranspiration (ET), (b) volumetric soil moisture (VSM), and (c) the Priestley–Taylor (PT) α simulated by CASA biogeochemical model with the improved ET algorithm, and (d) satellite-derived net radiation (R_{net}) at the Tonzi Savanna site from 2003 to 2005. The parameters used here for α were derived from an optimization of α inverted with tower-measured LE and MODIS-derived available energy. Tower measurements are shown in solid dot for comparison.

(2004), ET was calculated as the residual of total precipitation, the net stream flow from river discharge measurements, and the change in terrestrial water storage derived from Gravity Recovery and Climate Experiment (GRACE) satellite measurements during 2002–2003.

We calculated runoff as a residual between precipitation and ET, assuming there was no significant change in terrestrial water storage over a three year period. Our runoff estimate was 989 km^3 yr^{-1} for the Mississippi River basin from 2006 to 2008, which was similar to 918 km^3 yr^{-1} from MOD16, and higher than the historical gauge-based estimate of 513 km^3 yr^{-1} by Perry et al. (1996). The runoff from Fisher et al. (2008) was much smaller, averaging 216 km^3 yr^{-1} during 1986–1993. We calculated the runoff based on the USGS gauge observations at Vicksburg, Mississippi (07289000) in 2008, using the algorithm from (Maurer & Lettenmaier, 2001). The algorithm included an extrapolation based on the drainage areas. The estimated runoff in 2008 was 846 km^3 yr^{-1}. The runoff from the CASA ET estimate in 2008 was 1034 km^3 yr^{-1}.

Runoff from the Mississippi River basin was positive in fall and winter, declined from February/March until summer, when ET exceeded precipitation (Fig. 8b). Our precipitation minus ET (P–ET) averaged over the Mississippi River basin ranged from −1.1 mm/day in July to 2.2 mm/day in winter. Mean annual P–ET was 0.78 mm/day. P–ET derived from GRACE storage and GPCP precipitation combined with river discharge data in the Mississippi River basin showed a similar seasonal pattern and an average P–ET of 0.49 mm/day for 2002 and 2003 (Swenson & Wahr, 2006). The derived monthly runoff from the Vicksburg station in 2008 also had a strong seasonal pattern, with a minimum of 0.27 mm/day in November and a maximum of 1.56 mm/day in April, and a mean annual rate of 0.72 mm/day.

The 2006–2008 runoff for the Columbia River basin based on PRISM precipitation and our ET estimates was 261 km^3 yr^{-1}, which compared reasonably with 235 km^3 yr^{-1} derived from the historical gauge measurements (Perry et al., 1996), and was similar with 263 km^3 yr^{-1} from MOD16 (Mu et al., 2007).

4. Discussion

4.1. Spatial distribution of ET and its controlling factors

The spatial pattern of ET followed those of R_{net} and α at a continental scale, i.e., a decreasing trend from southeast to northwest and relatively high values in the northwest coastal areas (Fig. 9). We summarized the mean annual ET during 2006–2008 as a function of land cover type in Table 6 (see Fig. S4 for the land cover map from Friedl et al. (2002)). Evergreen broadleaf forests had the highest mean annual ET (840 ± 234 mm yr^{-1}), while shrublands (231 ± 123 mm yr^{-1}) and barren or sparsely vegetated areas (110 ± 76 mm yr^{-1}) were lower. R_{net} decreased from 125 ± 9 W m^{-2} in evergreen broadleaf forests to 54 ± 15 W m^{-2} in shrublands, and 39 ± 16 W m^{-2} in deserts. The relative change of R_{net} among land cover types was much smaller than that of ET. The lower PT coefficient due to lower leaf area index and soil water content contributed further to the decreasing ET with decreasing vegetation cover. Mean annual α ranged from 0.72 (±0.20) in broadleaf forest, 0.45 (±0.15) in shrublands, to 0.36 (±0.11) in barren areas.

ET followed the pattern of precipitation on a large scale (Fig. 10a). ET increased linearly with precipitation to a mean annual precipitation (MAP) of ~900 mm yr^{-1}, reaching a maximum of 672 mm yr^{-1} at a MAP of ~1450 mm yr^{-1}. ET decreased at higher precipitation, probably as a consequence of increased cloud cover and lower radiation (Fig. 10b). Mean annual R_{net} increased with precipitation gradually from 44 to 96 W m^{-2} at a MAP of ~1400 mm yr^{-1}, decreased to 78 W m^{-2} at a MAP of ~1600 mm yr^{-1}, and stayed almost constant around 78 W m^{-2} above 1600 mm yr^{-1} (Fig. 10b). The α coefficient increased rapidly with precipitation until MAP reached 400 mm yr^{-1} (Fig. 10c). α was the main driver for the spatial variation of ET when MAP is below 400 mm yr^{-1}, with a correlation coefficient of 0.81. R_{net} was less well correlated with ET (r = 0.52). R_{net} was the main driver (r = 0.86) for areas with MAP greater than 400 mm yr^{-1}. Mean annual runoff increased with increasing precipitation (Fig. 10d). This is consistent with the theory of supply and demand for water (Budyko, 1974; Federer, 1982) where ET is limited by the supply of water from the roots or by atmospheric water demand (PET, primarily driven by radiation). When there is limited supply of soil moisture, ET is modulated significantly by available water and canopy characteristics (Baldocchi & Xu, 2007; Ryu et al., 2008). In contrast, over areas or during periods with an unlimited soil moisture, ET is more closely regulated by the energy available to drive evaporation (Jarvis & Mcnaughton, 1986; Ryu et al., 2008).

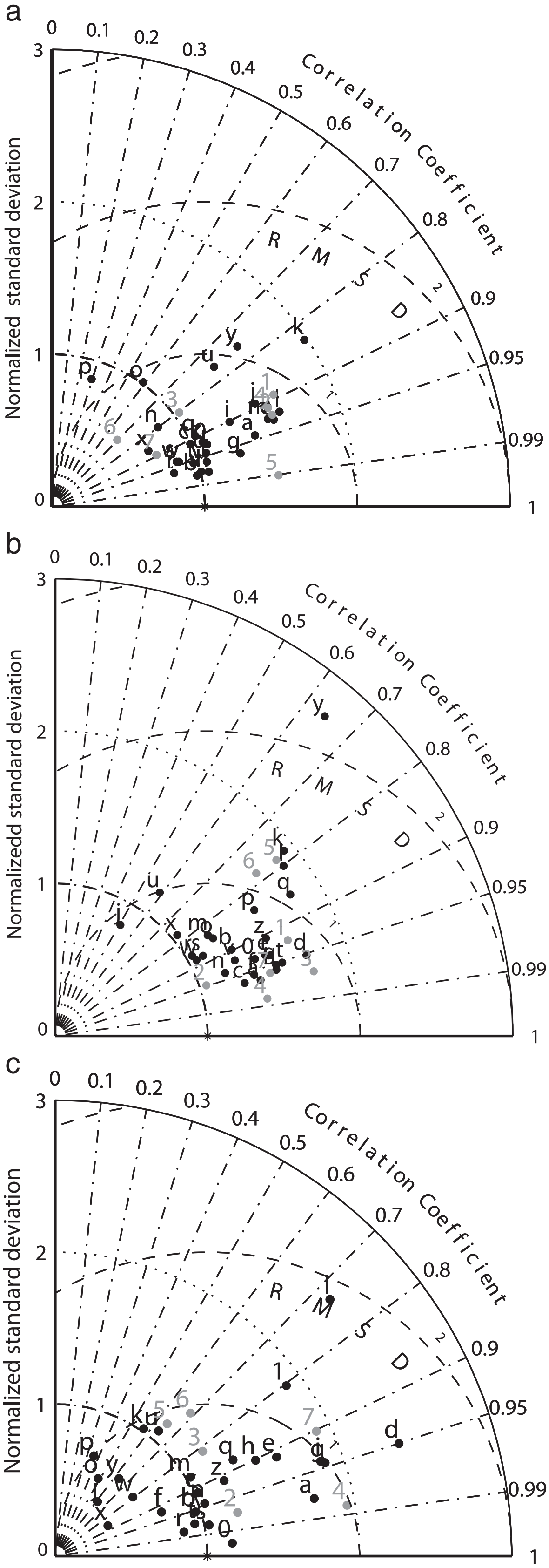

Fig. 7. Taylor diagram for ET over 27 optimization sites (a to z, 0) and 7 validation sites (1 to 7) from (a) the improved CASA ET algorithm (b) the original CASA ET algorithm, and (c) MOD16. The radial distance from the origin is proportional to the standard deviation of the estimate normalized by the standard deviation of the observations, the azimuthal position gives the correlation coefficient, and the radial distance from the reference point is proportional to the centered RMSE difference between the modeled and observed time series normalized by the reference standard deviation. Data used here are from 2006 to 2008.

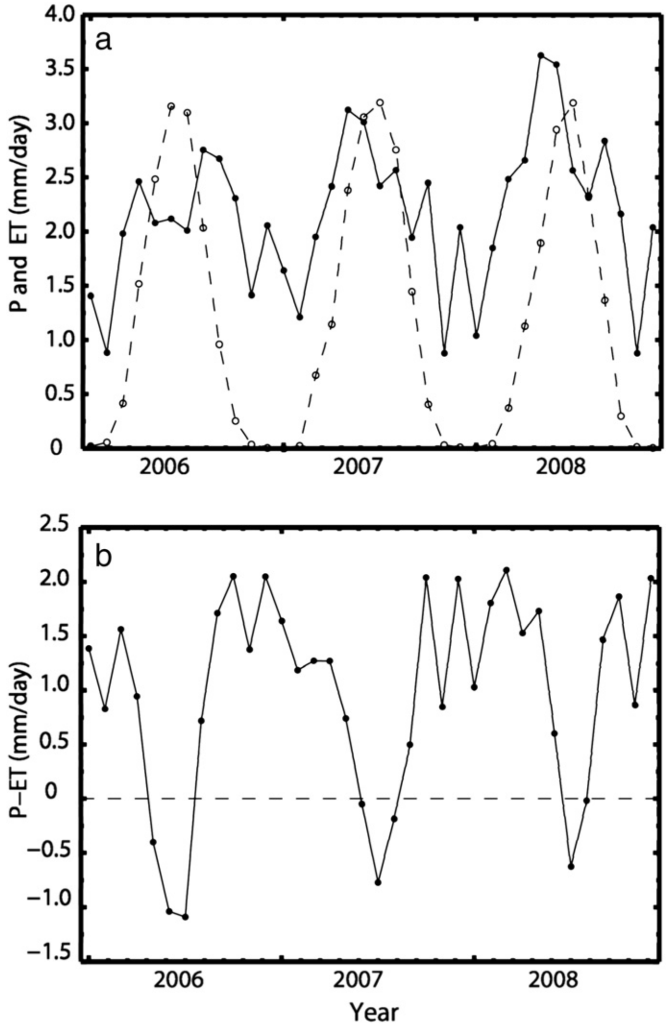

Fig. 8. Time series of basin-scale monthly precipitation (solid dots) and evapotranspiration (open circles) (a), and precipitation minus ET rate (b) for the Mississippi River basin from 2006 to 2008.

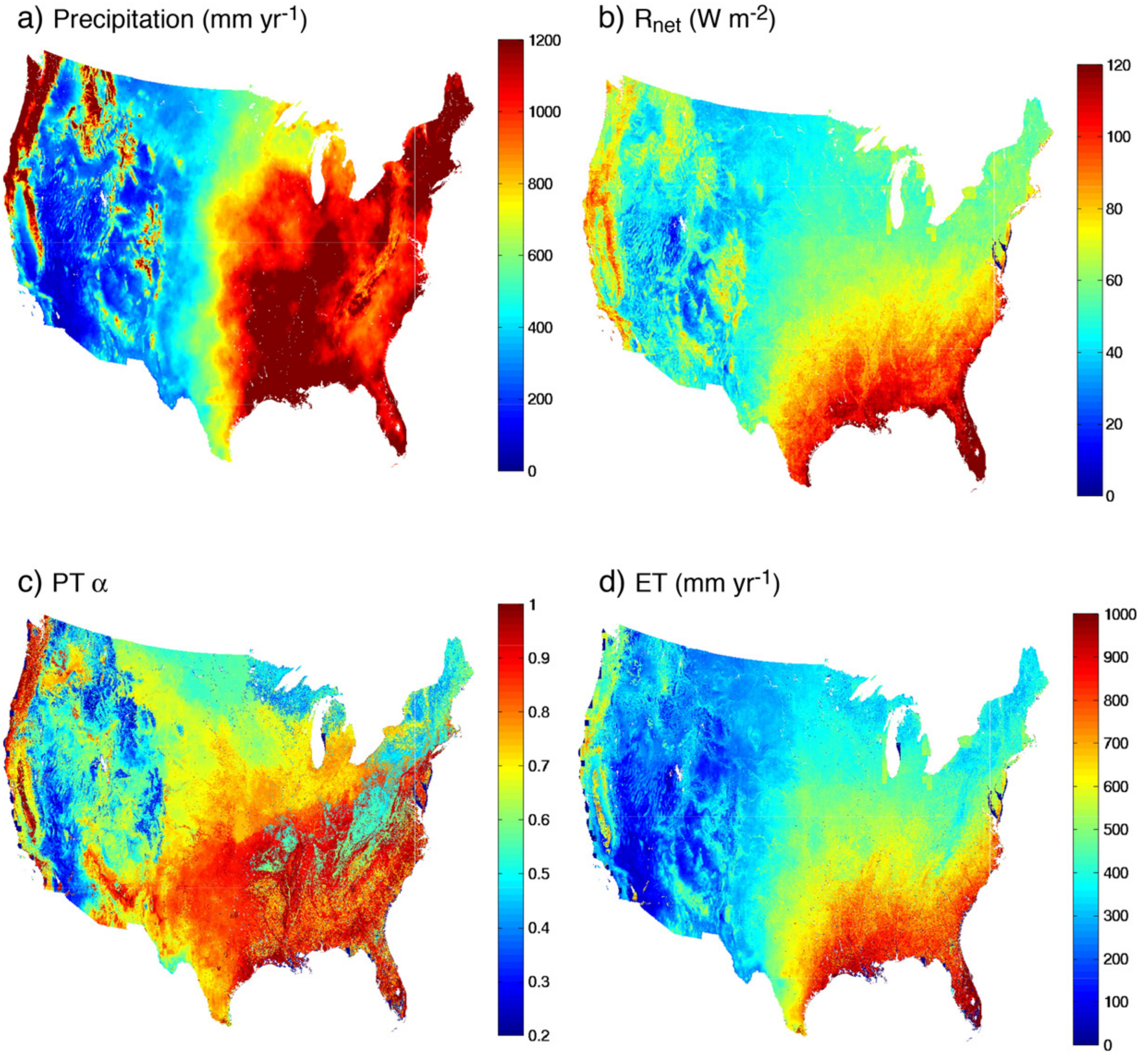

Fig. 9. Spatial distribution of annual mean monthly (a) precipitation, (b) MODIS-derived net radiation, (c) the Priestley–Taylor α coefficient, and (d) ET from improved CASA model, averaged from 2006 to 2008 across the conterminous United States.

4.2. Interannual variation

Barren or sparsely vegetated areas showed the largest interannual variation in ET among vegetation types during 2006 and 2008, with a standard deviation around 10% of the mean value (Table 6). R_{net} varied by ~7%, and PT α varied by 2% in these areas. Spatially, southern Texas and southern California experienced the largest interannual variation in ET (~20% of mean ET), where PT coefficient varied by more than 15% and R_{net} only varied by a few percent. Interannual variation of ET in desert ecosystems also varied substantially. Interannual variability in R_{net} in the Marine ecoregion (Fig. S4) also was large (around 7%), and the PT coefficient variation further amplified the interannual variation in ET to around 10% (Table S2). The majority of the eastern US showed little interannnual variation in ET, R_{net}, and α.

4.3. Ecophysiological basis for parameterization of the PT α coefficient

Evapotranspiration is controlled by both climatic and biological processes. The coupling between climate and ecosystems complicates the analysis of the mechanisms controlling ET. The relative importance of factors such as available energy, soil moisture supply, ecological and physiological control by plants, and the demand by the atmosphere, varies across ecosystems. The competing role of these factors makes the estimate of ET at regional or global scales challenging. According to the Omega theory (Jarvis & Mcnaughton, 1986), ET is proportional to equilibrium ET (which is a function of available energy) and is relatively independent of surface control over well-watered or aerodynamically-smooth vegetation. In contrast, tall vegetation like forests is more coupled to the atmosphere and ET is controlled more by vegetation characteristics.

We hypothesize that available energy is the first order controller of ET and the functional and environmental variables are of secondary importance. At the leaf level, stomatal conductance is reduced when soil moisture is limited. At the canopy level, vegetation structure, including LAI, responds to temperature and precipitation, which in turn affects actual ET. Our method did not model surface resistance directly; instead, it was implicitly considered during the optimization of the PT α coefficient as a function of LAI and soil moisture. We further hypothesize that LAI responds to soil drought and stomatal closure in a way that is consistent with plants under stress adjusting their leaf density to optimize their resource utilization (Field et al., 1995).

Our analysis shows that soil moisture in some cases explains additional variance in ET beyond LAI, and thus an explicit function of soil moisture is useful in parameterizing moisture controls on ET. This approach is complementary to VPD-based approaches (Mu et al.,

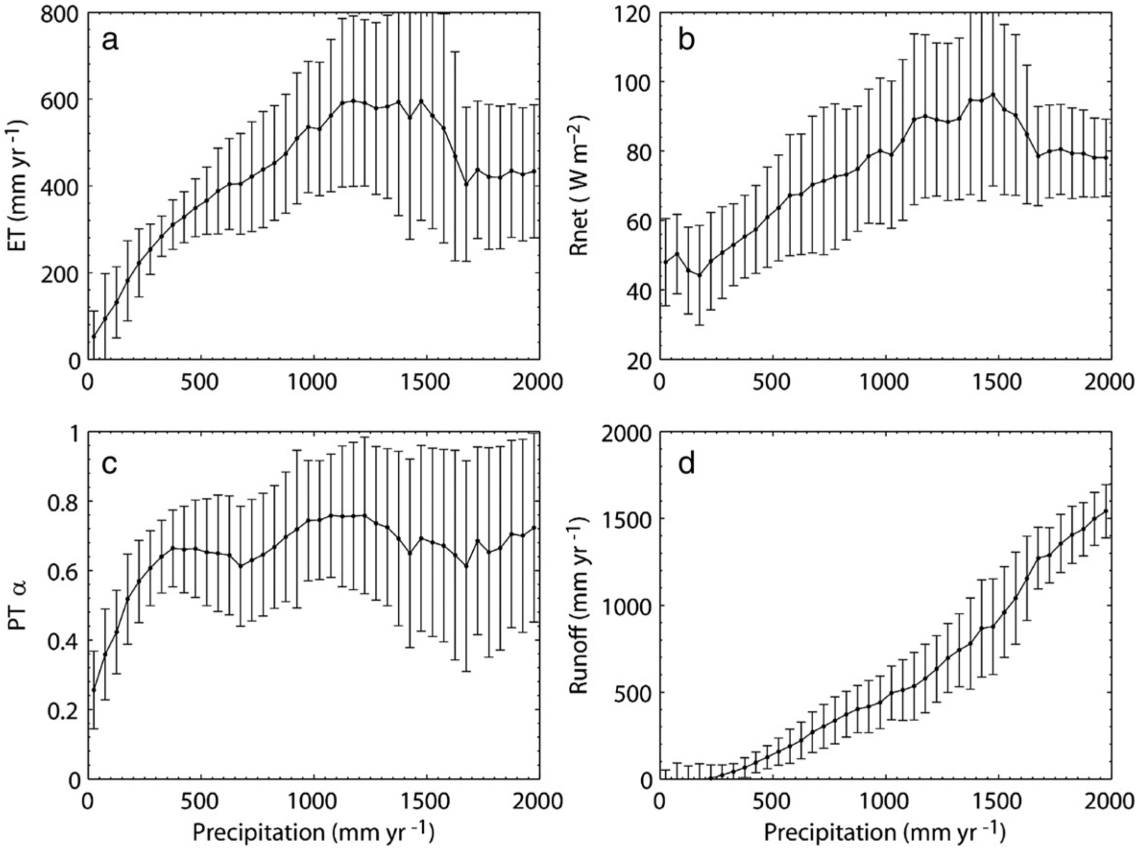

Fig. 10. Relationship between ET, R_{net}, the Priestley–Taylor α coefficient, and runoff with precipitation averaged from 2006 to 2008 across the conterminous United States.

2007), and may be of use when VPD information is unavailable. We assume that soil moisture is linked to and reflects the evaporative demand of the atmosphere, especially at midday when convection is the strongest due to strong vertical mixing.

The exponential LAI term in Eq. (7) accounts for potential non-linearities between LAI and α (and also ET) and has the effect of causing α to level off at high LAI values. We did another two sets of optimization (linear and exponential) using MODIS EVI (but with the same factor for representing soil moisture stress) over the 27 primary sites used in our analysis, and found the EVI-based optimizations had slightly lower Taylor scores of 0.78 (for the linear model) and 0.77 (for an exponential model). Thus, although ET is more linearly related to VIs (Choudhury et al., 1994; Glenn et al., 2010), our optimization with LAI yielded comparable results.

4.4. ET and runoff at a continental river basin scale

Our understanding and quantification of water budget in both atmosphere and terrestrial biosphere is limited by a lack of observational data and by inadequate parameterizations of the underlying physics in hydrology models. ET is considered the most uncertain component in water budget (Lettenmaier & Famiglietti, 2006). At basin to continental scales, runoff has been mostly derived from gauge-based river discharge observations, model simulations, atmospheric moisture budgets (from reanalysis), and from GRACE satellite measurements, either alone or combined with other measurements described above (Rodell et al., 2004). On interannual time scales, precipitation minus ET over land can be used as a proxy for runoff, assuming negligible storage changes. Our approach for estimating regional ET has potential

Table 6
Mean ET, R_{net}, Priestley–Taylor α, and precipitation and their interannual variability (IAV) averaged over different vegetation types in the conterminous United States (CONUS).

	Mean ± STD					IAV (2006~2008)			
	Area (km^2)	ET ($mm\ yr^{-1}$)	R_{net} ($W\ m^{-2}$)	α	Precip ($mm\ yr^{-1}$)	ET	R_{net}	α (% of mean)	Precip
Evergreen Needleleaf Forest	502,617	370 ± 169	79 ± 13	0.5 ± 0.2	1078 ± 642	9.3	5.8	3.5	11.3
Evergreen Broadleaf Forest	23,351	840 ± 234	125 ± 9	0.7 ± 0.2	1168 ± 184	5.0	4.3	1.4	5.7
Deciduous Needleleaf Forest	3222	271 ± 158	73 ± 20	0.3 ± 0.1	859 ± 363	4.8	2.9	1.8	1.9
Deciduous Broadleaf Forest	546,330	474 ± 108	76 ± 11	0.5 ± 0.1	1057 ± 190	3.1	2.5	1.1	6.4
Mixed Forests	498,751	696 ± 238	90 ± 22	0.7 ± 0.2	1086 ± 301	3.9	3.7	0.4	6.0
Shrublands	931,985	231 ± 123	54 ± 15	0.5 ± 0.1	295 ± 185	1.0	2.9	0.7	1.9
Savannas and Grasslands	2,529,156	391 ± 176	64 ± 22	0.6 ± 0.1	546 ± 306	4.7	4.2	1.1	5.7
Croplands	2,480,986	574 ± 195	73 ± 19	0.7 ± 0.2	892 ± 269	3.4	2.6	2.6	4.5
Barren or Sparsely Vegetated	83,732	110 ± 76	39 ± 16	0.4 ± 0.1	157 ± 184	9.6	7.4	2.3	5.5
CONUS	7,600,130	454 ± 191	69 ± 21	0.6 ± 0.2	733 ± 420	4.0	3.5	1.6	5.3

applications for runoff estimates by integrating satellite data and eddy-covariance measurements. The value of MODIS derived ET is likely to increase in the future, with longer time series reducing uncertainties associated with year-to-year changes in water storage. However, water storage change may still be a significant term in some areas where ground aquifers are being rapidly depleted (e.g., Rodell et al.,2009) thus requiring multi-faceted approaches for closing the water budget that draw upon multiple data streams.

5. Conclusions

We estimated regional net radiation at 1 km by 1 km resolution using satellite observations including MODIS surface albedo and land surface temperature and GOES incoming solar radiation. Good agreement was found between satellite-based estimates of monthly net radiation (R_{net}) and field-measured R_{net}, with a RMSE of less than 30 W m^{-2}.

We developed an empirical ET algorithm using AmeriFlux data and MODIS LAI to improve the estimation of ET and thus soil moisture in the CASA biogeochemical model at a regional scale. The coefficient α in the semi-empirical Priestley–Taylor (PT) ET approach was parameterized with leaf area index and soil moisture at a monthly time step using observations from 27 AmeriFlux sites. The optimization at a PFT level performed well with a RMSE of 16 W m^{-2} for predicted monthly LE, a correlation of 0.90 with tower measured LE, and a mean Taylor score of 0.80 when averaged over all the optimization sites.

We implemented the PT-based ET algorithm in CASA, with soil moisture simulated by CASA, MODIS LAI, and regional R_{net} estimated with satellite observations. The estimated seasonal ET agreed well with the tower measurements. The RMSE was reduced from 27.1 mm mon^{-1} from the Thornwaite ET in the original version to 21.1 mm mon^{-1} with our improved approach. The Taylor score increased from 0.68 to 0.73 averaged over all 27 optimization sites plus the 7 sites used for validation. Mean biases also were reduced. Our ET algorithm performed better than the current version of the MOD16 ET product for which RMSE was 26.5 mm/day and the Taylor score was 0.62.

The spatial distribution of our modeled mean annual ET at 1 km resolution followed the patterns of vegetation distribution, R_{net} and precipitation. Our ET estimates ranged from 110 mm yr^{-1} in barren or sparsely vegetated areas to 840 mm yr^{-1} in evergreen broadleaf forest. The PT α coefficient was related to precipitation when MAP was less than 400 mm yr^{-1}, and was the main driver for the spatial variation of ET with a correlation of 0.81. R_{net} was the main driver for the spatial distribution of ET when MAP was higher than 400 mm. The ET rate averaged over the Mississippi River basin varied from 0 in January to 3.5 mm/day in June/July, in good agreement with the results from Rodell et al. (2004) derived using GRACE satellite measurements and river discharge. Runoff from the Mississippi basins was comparable with that from MOD16 ET data.

The sensitivity of LE to available energy plays an important role in the response of surface temperature to increasing surface radiative forcing. Our study showed that relative importance of available energy and the PT α coefficient (regulated by LAI and soil moisture) in controlling LE varied considerably across the CONUS. Our estimates provide information for comparing and calibrating climate models in terms of their sensitivity to available energy (Winter & Eltahir, 2010). Drought affects photosynthesis and heterotrophic respiration in many ecosystems. An important next step is to extend our analysis to quantify how the soil moisture affects net ecosystem CO_2 exchange in various ecosystems.

Acknowledgments

This work was supported by NASA grants to Y. Jin (NNX08AR69G), M. Goulden (NNG05GD12G) and J. Randerson (NNX08AF64G). The authors are grateful to Q. Mu for providing us the updated MODIS ET data, to J. Fisher for providing us AVHRR ET data, to M. Rodell for discussions on the Mississippi River basin runoff estimates from GRACE observations, and to Z.-L. Yang for suggestions on soil parameters. We thank two anonymous reviewers for their thoughtful and constructive comments and to G.J. Collatz for discussions on improving the CASA model. We would like to thank all the AmeriFlux principal investigators for making the tower data available to us.

Appendix A. Supplementary data

Supplementary data to this article can be found online at doi:10.1016/j.rse.2011.04.031.

References

Albertson, J. D., Katul, G. G., & Wiberg, P. (2001). Relative importance of local and regional controls on coupled water, carbon, and energy fluxes. *Advances in Water Resources*, *24*, 1103–1118.

Baldocchi, D., Falge, E., Gu, L. H., Olson, R., Hollinger, D., et al. (2001). FLUXNET: A new tool to study the temporal and spatial variability of ecosystem-scale carbon dioxide, water vapor, and energy flux densities. *Bulletin of the American Meteorological Society*, *82*, 2415–2434.

Baldocchi, D. D., & Xu, L. K. (2007). What limits evaporation from Mediterranean oak woodlands — The supply of moisture in the soil, physiological control by plants or the demand by the atmosphere? *Advances in Water Resources*, *30*, 2113–2122. doi:10.1016/J.Advwatres.2006.06.013.

Baldocchi, D. D., Xu, L. K., & Kiang, N. (2004). How plant functional-type, weather, seasonal drought, and soil physical properties alter water and energy fluxes of an oak-grass savanna and an annual grassland. *Agricultural and Forest Meteorology*, *123*, 13–39. doi:10.1016/J.Agrformet.2003.11.006.

Bastiaanssen, W. G. M., Menenti, M., Feddes, R. A., & Holtslag, A. A. M. (1998). A remote sensing Surface Energy Balance Algorithm for Land (SEBAL) — 1. Formulation. *Journal of Hydrology*, *213*, 198–212.

Bastiaanssen, W. G. M., Pelgrum, H., Wang, J., Ma, Y., Moreno, J. F., et al. (1998). A remote sensing surface energy balance algorithm for land (SEBAL) — 2. Validation. *Journal of Hydrology*, *213*, 213–229.

Baumgartner, A., & Reichel, E. (1975). *The world water balance: Mean annual global, continental and maritime precipitation, evaporation and run-off.* Amsterdam, New York: Elsevier Scientific Pub. Co.

Bolstad, P. V., Davis, K. J., Martin, J., Cook, B. D., & Wang, W. (2004). Component and whole-system respiration fluxes in northern deciduous forests. *Tree Physiology*, *24*, 493–504.

Bonan, G.B. (1996). A Land Surface MODEK (LSM version 1.0) for ecological, hydrological, and atmospheric studies: Technical description and user's guide. In. Boulder, CO.

Budyko, M. I. (1974). *Climate and life.* New York, NY: Academic Press.

Campbell, G. S., & Norman, J. M. (1998). *An introduction to environmental biophysics.* New York: Springer-Verlag.

Chen, J. Q., Paw, U, K. T., Ustin, S. L., Suchanek, T. H., Bond, B. J., et al. (2004). Net ecosystem exchanges of carbon, water, and energy in young and old-growth Douglas-fir forests. *Ecosystems*, *7*, 534–544. doi:10.1007/S10021-004-0143-6.

Choudhury, B. J., Ahmed, N. U., Idso, S. B., Reginato, R. J., & Daughtry, C. S. T. (1994). Relations between evaporation coefficients and vegetation indexes studied by model simulations. *Remote Sensing of Environment*, *50*, 1–17.

Choudhury, B. J., & DiGirolamo, N. E. (1998). A biophysical process-based estimate of global land surface evaporation using satellite and ancillary data — I. Model description and comparison with observations. *Journal of Hydrology*, *205*, 164–185.

Cleugh, H. A., Leuning, R., Mu, Q. Z., & Running, S. W. (2007). Regional evaporation estimates from flux tower and MODIS satellite data. *Remote Sensing of Environment*, *106*, 285–304. doi:10.1016/J.Rse.2006.07.007.

Coleman, T. F., & Li, Y. Y. (1996). An interior trust region approach for nonlinear minimization subject to bounds. *Siam Journal on Optimization*, *6*, 418–445.

Coulter, R. L, Pekour, M. S., Cook, D. R., Klazura, G. E., Martin, T. J., et al. (2006). Surface energy and carbon dioxide fluxes above different vegetation types within ABLE. *Agricultural and Forest Meteorology*, *136*, 147–158. doi:10.1016/J.Agrformet.2004.11.011.

Dahm, C. N., Cleverly, J. R., Coonrod, J. E. A., Thibault, J. R., McDonnell, D. E., et al. (2002). Evapotranspiration at the land/water interface in a semi-arid drainage basin. *Freshwater Biology*, *47*, 831–843.

Daly, C., Halbleib, M., Smith, J. I., Gibson, W. P., Doggett, M. K., et al. (2008). Physiographically sensitive mapping of climatological temperature and precipitation across the conterminous United States. *International Journal of Climatology*, *28*, 2031–2064. doi:10.1002/Joc.1688.

Davis, K. J., Bakwin, P. S., Yi, C. X., Berger, B. W., Zhao, C. L., et al. (2003). The annual cycles of CO_2 and H_2O exchange over a northern mixed forest as observed from a very tall tower. *Global Change Biology*, *9*, 1278–1293.

Desai, A. R., Bolstad, P. V., Cook, B. D., Davis, K. J., & Carey, E. V. (2005). Comparing net ecosystem exchange of carbon dioxide between an old-growth and mature forest in the upper Midwest, USA. *Agricultural and Forest Meteorology*, *128*, 33–55. doi:10.1016/J.Agrformet.2004.09.005.

Duarte, H. F., Dias, N. L., & Maggiotto, S. R. (2006). Assessing daytime downward longwave radiation estimates for clear and cloudy skies in Southern Brazil. *Agricultural and Forest Meteorology*, *139*, 171–181. doi:10.1016/J.Agrformet.2006.06.008.

Eichinger, W. E., Parlange, M. B., & Stricker, H. (1996). On the concept of equilibrium evaporation and the value of the Priestley–Taylor coefficient. *Water Resources Research*, *32*, 161–164.

Federer, C. A. (1982). Transpirational supply and demand — Plant, soil, and atmospheric effects evaluated by simulation. *Water Resources Research*, *18*, 355–362.

Field, C. B., Randerson, J. T., & Malmstrom, C. M. (1995). Global net primary production — Combining ecology and remote-sensing. *Remote Sensing of Environment*, *51*, 74–88.

Fisher, J. B., Tu, K. P., & Baldocchi, D. D. (2008). Global estimates of the land–atmosphere water flux based on monthly AVHRR and ISLSCP-II data, validated at 16 FLUXNET sites. *Remote Sensing of Environment*, *112*, 901–919. doi:10.1016/J.Rse.2007.06.025.

Friedl, M. A., McIver, D. K., Hodges, J. C. F., Zhang, X. Y., Muchoney, D., et al. (2002). Global land cover mapping from MODIS: Algorithms and early results. *Remote Sensing of Environment*, *83*, 287–302 Pii S0034-4257(02)00078-0.

Gillies, R. R., Carlson, T. N., Cui, J., Kustas, W. P., & Humes, K. S. (1997). A verification of the 'triangle' method for obtaining surface soil water content and energy fluxes from remote measurements of the Normalized Difference Vegetation Index (NDVI) and surface radiant temperature. *International Journal of Remote Sensing*, *18*, 3145–3166.

Gilmanov, T. G., Tieszen, L. L., Wylie, B. K., Flanagan, L. B., Frank, A. B., et al. (2005). Integration of CO_2 flux and remotely-sensed data for primary production and ecosystem respiration analyses in the Northern Great Plains: Potential for quantitative spatial extrapolation. *Global Ecology and Biogeography*, *14*, 271–292. doi:10.1111/J.1466-822x.2005.00151.X.

Glenn, E. P., Nagler, P. L., & Huete, A. R. (2010). Vegetation index methods for estimating evapotranspiration by remote sensing. *Surveys in Geophysics*, *31*, 531–555. doi:10.1007/S10712-010-9102-2.

Gu, L., Meyers, T., Pallardy, S. G., Hanson, P. J., Yang, B., Heuer, M., Hosman, K. P., Riggs, J. S., Sluss, D., & Wullschleger, S. D. (2006). Direct and indirect effects of atmospheric conditions and soil moisture on surface energy partitioning revealed by a prolonged drought at a temperate forest site. *J. Geophys. Res.*, *111*, D16102. doi:10.1029/2006JD007161.

Hadley, J. L., Kuzeja, P. S., Daley, M. J., Phillips, N. G., Mulcahy, T., et al. (2008). Water use and carbon exchange of red oak- and eastern hemlock-dominated forests in the northeastern USA: Implications for ecosystem-level effects of hemlock woolly adelgid. *Tree Physiology*, *28*, 615–627.

Hollinger, D. Y., Aber, J., & Dail, B. (2004). Spatial and temporal variability in forest–atmosphere CO_2 exchange (vol 10, pg 1689, 2004). *Global Change Biology*, *10*, 1689–1706.

Hollinger, S. E., Bernacchi, C. J., & Meyers, T. P. (2005). Carbon budget of mature no-till ecosystem in North Central Region of the United States. *Agricultural and Forest Meteorology*, *130*, 59–69.

Houborg, R., Anderson, M. C., Norman, J. M., Wilson, T., & Meyers, T. (2009). Intercomparison of a 'bottom-up' and 'top-down' modeling paradigm for estimating carbon and energy fluxes over a variety of vegetative regimes across the US. *Agricultural and Forest Meteorology*, *149*, 1875–1895. doi:10.1016/J.Agrformet.2009.06.014.

Jarvis, P. G., & Mcnaughton, K. G. (1986). Stomatal control of transpiration — Scaling up from leaf to region. *Advances in Ecological Research*, *15*, 1–49.

Jenkins, J. P., Richardson, A. D., Braswell, B. H., Ollinger, S. V., Hollinger, D. Y., et al. (2007). Refining light-use efficiency calculations for a deciduous forest canopy using simultaneous tower-based carbon flux and radiometric measurements. *Agricultural and Forest Meteorology*, *143*, 64–79. doi:10.1016/J.Agrformet.2006.11.008.

Jiang, L., & Islam, S. (2001). Estimation of surface evaporation map over southern Great Plains using remote sensing data. *Water Resources Research*, *37*, 329–340.

Jin, M. L., & Liang, S. L. (2006). An improved land surface emissivity parameter for land surface models using global remote sensing observations. *Journal of Climate*, *19*, 2867–2881.

Jin, Y. F., Schaaf, C. B., Gao, F., Li, X. W., Strahler, A. H., et al. (2003). Consistency of MODIS surface bidirectional reflectance distribution function and albedo retrievals: 1. Algorithm performance. *Journal of Geophysical Research-Atmospheres*, *108*. doi:10.1029/2002jd002803 Artn 4158.

Jin, Y. F., Schaaf, C. B., Woodcock, C. E., Gao, F., Li, X. W., et al. (2003). Consistency of MODIS surface bidirectional reflectance distribution function and albedo retrievals: 2. Validation. *Journal of Geophysical Research-Atmospheres*, *108*. doi:10.1029/2002jd002804 Artn 4159.

Jung, M., Reichstein, M., & Bondeau, A. (2009). Towards global empirical upscaling of FLUXNET eddy covariance observations: Validation of a model tree ensemble approach using a biosphere model. *Biogeosciences*, *6*, 2001–2013.

Jung, M., Reichstein, M., Ciais, P., Seneviratne, S. I., Sheffield, J., et al. (2010). Recent decline in the global land evapotranspiration trend due to limited moisture supply. *Nature*, *467*, 951–954. doi:10.1038/Nature09396.

Kalma, J. D., & Jupp, D. L. B. (1990). Estimating evaporation from pasture using infrared thermometry — Evaluation of a one-layer resistance model. *Agricultural and Forest Meteorology*, *51*, 223–246.

Kalnay, E., Kanamitsu, M., Kistler, R., Collins, W., Deaven, D., et al. (1996). The NCEP/NCAR 40-year reanalysis project. *Bulletin of the American Meteorological Society*, *77*, 437–471.

Kurpius, M. R., Panek, J. A., Nikolov, N. T., McKay, M., & Goldstein, A. H. (2003). Partitioning of water flux in a Sierra Nevada ponderosa pine plantation. *Agricultural and Forest Meteorology*, *117*, 173–192. doi:10.1016/S1068-1923(03)00062-5.

Lettenmaier, D. P., & Famiglietti, J. S. (2006). Hydrology — Water from on high. *Nature*, *444*, 562–563. doi:10.1038/444562a.

Lu, X. L., & Zhuang, Q. L. (2010). Evaluating evapotranspiration and water-use efficiency of terrestrial ecosystems in the conterminous United States using MODIS and AmeriFlux data. *Remote Sensing of Environment*, *114*, 1924–1939. doi:10.1016/J.Rse.2010.04.001.

Matamala, R., Jastrow, J. D., Miller, R. M., & Garten, C. T. (2008). Temporal changes in C and N stocks of restored prairie: Implications for C sequestration strategies. *Ecological Applications*, *18*, 1470–1488.

Maurer, E. P., & Lettenmaier, D. P. (2001). *Calculation of undepleted runoff for the GCIP region, 1998–2000.* http://www.ce.washington.edu/~edm/WEBS_runoff/

Monteith, J. L. (1965). Evaporation and environment. *Symposium of the Society of Experimental Biology*, *19*, 205–224.

Mu, Q., Heinsch, F. A., Zhao, M., & Running, S. W. (2007). Development of a global evapotranspiration algorithm based on MODIS and global meteorology data. *Remote Sensing of Environment*, *111*, 519–536. doi:10.1016/J.Rse.2007.04.015.

Myneni, R. B., Hoffman, S., Knyazikhin, Y., Privette, J. L., Glassy, J., et al. (2002). Global products of vegetation leaf area and fraction absorbed PAR from year one of MODIS data. *Remote Sensing of Environment*, *83*, 214–231 Pii S0034-4257(02)00074-3.

Nagler, P. L., Glenn, E. P., & Thompson, T. L. (2003). Comparison of transpiration rates among saltcedar, cottonwood and willow trees by sap flow and canopy temperature methods. *Agricultural and Forest Meteorology*, *116*, 73–89. doi:10.1016/S0168-1923(02)00251-4.

Nagler, P. L., Scott, R. L., Westenburg, C., Cleverly, J. R., Glenn, E. P., et al. (2005). Evapotranspiration on western US rivers estimated using the Enhanced Vegetation Index from MODIS and data from eddy covariance and Bowen ratio flux towers. *Remote Sensing of Environment*, *97*, 337–351. doi:10.1016/J.Rse.2005.05.011.

Nishida, K., Nemani, R. R., Running, S. W., & Glassy, J. M. (2003). An operational remote sensing algorithm of land surface evaporation. *Journal of Geophysical Research-Atmospheres*, *108*. doi:10.1029/2002jd002062 Artn 4270.

Noormets, A., McNulty, S. G., DeForest, J. L., Sun, G., Li, Q., et al. (2008). Drought during canopy development has lasting effect on annual carbon balance in a deciduous temperate forest. *New Phytologist*, *179*, 818–828.

Oishi, A. C., Oren, R., & Stoy, P. C. (2008). Estimating components of forest evapotranspiration: A footprint approach for scaling sap flux measurements. *Agricultural and Forest Meteorology*, *148*, 1719–1732. doi:10.1016/J.Agrformet.2008.06.013.

Overgaard, J., Rosbjerg, D., & Butts, M. B. (2006). Land-surface modelling in hydrological perspective — A review. *Biogeosciences*, *3*, 229–241.

Perry, G. D., Duffy, P. B., & Miller, N. L. (1996). An extended data set of river discharges for validation of general circulation models. *Journal of Geophysical Research-Atmospheres*, *101*, 21339–21349.

Pervez, M. S., & Brown, J. F. (2010). Mapping irrigated lands at 250-m scale by merging MODIS data and national agricultural statistics. *Remote Sensing*, *2*, 2388–2412. doi:10.3390/rs2102388.

Pinker, R. T., Laszlo, I., Tarpley, J. D., & Mitchell, K. (2002). Geostationary satellite parameters for surface energy balance. *Earth's Atmosphere, Ocean and Surface Studies*, *30*, 2427–2432 Pii S0273-1177(02)00720-2.

Pinker, R. T., Tarpley, J. D., Laszlo, I., Mitchell, K. E., Houser, P. R., et al. (2003). Surface radiation budgets in support of the GEWEX Continental-Scale International Project (GCIP) and the GEWEX Americas Prediction Project (GAPP), including the North American Land Data Assimilation System (NLDAS) Project. *Journal of Geophysical Research-Atmospheres*, *108*. doi:10.1029/2002jd003301 Artn 8844.

Potter, C. S., Randerson, J. T., Field, C. B., Matson, P. A., Vitousek, P. M., et al. (1993). Terrestrial ecosystem production — A process model-based on global satellite and surface data. *Global Biogeochemical Cycles*, *7*, 811–841.

Powell, T. L., Starr, G., Clark, K. L., Martin, T. A., & Gholz, H. L. (2005). Ecosystem and understory water and energy exchange for a mature, naturally regenerated pine flatwoods forest in north Florida. *Canadian Journal of Forest Research-Revue Canadienne De Recherche Forestiere*, *35*, 1568–1580. doi:10.1139/X05-075.

Prata, A. J. (1996). A new long-wave formula for estimating downward clear-sky radiation at the surface. *Quarterly Journal of the Royal Meteorological Society*, *122*, 1127–1151.

Priestley, C. H., & Taylor, R. J. (1972). Assessment of surface heat flux and evaporation using large scale parameters. *Monthly Weather Review*, *100*, 81–92.

Rodell, M., Famiglietti, J. S., Chen, J., Seneviratne, S. I., Viterbo, P., et al. (2004). Basin scale estimates of evapotranspiration using GRACE and other observations. *Geophysical Research Letters*, *31*. doi:10.1029/2004gl020873 Artn L20504.

Rodell, M., Velicogna, I., & Famiglietti, J. S. (2009). Satellite-based estimates of groundwater depletion in India. *Nature*, *460*, 999-U980. doi:10.1038/Nature08238.

Roerink, G. J., Su, Z., & Menenti, M. (2000). S-SEBI: A simple remote sensing algorithm to estimate the surface energy balance. *Physics and Chemistry of the Earth, Part B: Hydrology, Oceans and Atmosphere*, *25*, 147–157.

Ryu, Y., Baldocchi, D. D., Ma, S., & Hehn, T. (2008). Interannual variability of evapotranspiration and energy exchange over an annual grassland in California. *Journal of Geophysical Research-Atmospheres*, *113*. doi:10.1029/2007jd009263 Artn D09104.

Schaaf, C. B., Gao, F., Strahler, A. H., Lucht, W., Li, X. W., et al. (2002). First operational BRDF, albedo nadir reflectance products from MODIS. *Remote Sensing of Environment*, *83*, 135–148 Pii S0034-4257(02)00091-3.

Schwarz, P. A., Law, B. E., Williams, M., Irvine, J., Kurpius, M., et al. (2004). Climatic versus biotic constraints on carbon and water fluxes in seasonally drought-affected ponderosa pine ecosystems. *Global Biogeochemical Cycles*, *18*. doi:10.1029/2004gb002234 Artn Gb4007.

Scott, R. L., Huxman, T. E., Williams, D. G., & Goodrich, D. C. (2006). Ecohydrological impacts of woody-plant encroachment: seasonal patterns of water and carbon dioxide exchange within a semiarid riparian environment. *Global Change Biology*, *12*, 311–324. doi:10.1111/J.1365-2486.2005.01093.X.

Sims, P. L., & Bradford, J. A. (2001). Carbon dioxide fluxes in a southern plains prairie. *Agricultural and Forest Meteorology*, *109*, 117–134.

Sims, D. A., Rahman, A. F., Cordova, V. D., El-Masri, B. Z., Baldocchi, D. D., et al. (2008). A new model of gross primary productivity for North American ecosystems based solely on the enhanced vegetation index and land surface temperature from MODIS. *Remote Sensing of Environment*, *112*, 1633–1646. doi:10.1016/J.Rse.2007.08.004.

Stackhouse, J. P. W., Gupta, S. K., XCox, S. J., Mikovitz, J. C., & Zhang, T. (2010). Assessing uncertainties and variability in global and regional radiative budgets from the

NASA/GEWEX Surface Radiation Budget (SRB) Release-3.0 dataset. *13th Conference of Atmospheric Radiation. Portland, OR*.

Su, Z. (2002). The Surface Energy Balance System (SEBS) for estimation of turbulent heat fluxes. *Hydrology and Earth System Sciences*, *6*, 85–99.

Su, Z., Schmugge, T., Kustas, W. P., & Massman, W. J. (2001). An evaluation of two models for estimation of the roughness height for heat transfer between the land surface and the atmosphere. *Journal of Applied Meteorology*, *40*, 1933–1951.

Sumner, D. M., & Jacobs, J. M. (2005). Utility of Penman–Monteith, Priestley–Taylor, reference evapotranspiration, and pan evaporation methods to estimate pasture evapotranspiration. *Journal of Hydrology*, *308*, 81–104. doi:10.1016/J.Jhydrol.2004.10.023.

Sun, D., & Pinker, R. T. (2005). Implementation of GOES-based land surface temperature diurnal cycle to AVHRR. *International Journal of Remote Sensing*, *26*, 3975–3984. doi:10.1080/01431160500117634.

Swenson, S., & Wahr, J. (2006). Estimating large-scale precipitation minus evapotranspiration from GRACE satellite gravity measurements. *Journal of Hydrometeorology*, *7*, 252–270.

Taylor, K. E. (2001). Summarizing multiple aspects of model performance in a single diagram. *Journal of Geophysical Research-Atmospheres*, *106*, 7183–7192.

Thornthwaite, C. W. (1948). An approach toward a rational classification of climate. *Geographical Review*, *38*, 55–94.

Urbanski, S., Barford, C., Wofsy, S., Kucharik, C., Pyle, E., et al. (2007). Factors controlling CO_2 exchange on timescales from hourly to decadal at Harvard Forest. *Journal of Geophysical Research-Biogeosciences*, *112*. doi:10.1029/2006jg000293 Artn G02020.

Verstraeten, W. W., Veroustraete, F., & Feyen, J. (2005). Estimating evapotranspiration of European forests from NOAA-imagery at satellite overpass time: Towards an operational processing chain for integrated optical and thermal sensor data products. *Remote Sensing of Environment*, *96*, 256–276. doi:10.1016/J.Rse.2005.03.004.

Verstraeten, W. W., Veroustraete, F., & Feyen, J. (2008). Assessment of evapotranspiration and soil moisture content across different scales of observation. *Sensors*, *8*, 70–117.

Wan, Z. M. (2008). New refinements and validation of the MODIS Land-Surface Temperature/Emissivity products. *Remote Sensing of Environment*, *112*, 59–74. doi:10.1016/J.Rse.2006.06.026.

Wang, K. C., Dickinson, R. E., Wild, M., & Liang, S. L. (2010). Evidence for decadal variation in global terrestrial evapotranspiration between 1982 and 2002: 1. Model development. *Journal of Geophysical Research-Atmospheres*, *115*. doi:10.1029/2009jd013671 Artn D20112.

Wharton, S., Schroeder, M., Bible, K., Falk, M., & Paw, K. T. (2009). Stand-level gas-exchange responses to seasonal drought in very young versus old Douglas-fir forests of the Pacific Northwest, USA. *Tree Physiology*, *29*, 959–974. doi:10.1093/Treephys/Tpp 039.

Wielicki, B. A. (1996). Clouds and the Earth's radiant energy system (CERES): An earth observing system experiment (vol 77, pg 860, 1996). *Bulletin of the American Meteorological Society*, *77*, 1590-1590.

Wielicki, B. A., Barkstrom, B. R., Baum, B. A., Charlock, T. P., Green, R. N., et al. (1998). Clouds and the Earth's Radiant Energy System (CERES): Algorithm overview. *IEEE Transactions on Geoscience and Remote Sensing*, *36*, 1127–1141.

Winter, J. M., & Eltahir, E. A. B. (2010). The sensitivity of latent heat flux to changes in the radiative forcing: A framework for comparing models and observations. *Journal of Climate*, *23*, 2345–2356. doi:10.1175/2009jcli3158.1.

Yang, Z. L., Dickinson, R. E., Shuttleworth, W. J., & Shaikh, M. (1998). Treatment of soil, vegetation and snow in land surface models: A test of the biosphere–atmosphere transfer scheme with the HAPEX-MOBILHY, ABRACOS and Russian data. *Journal of Hydrology*, *213*, 109–127.

Yang, F. H., White, M. A., Michaelis, A. R., Ichii, K., Hashimoto, H., et al. (2006). Prediction of continental-scale evapotranspiration by combining MODIS and AmeriFlux data through support vector machine. *IEEE Transactions on Geoscience and Remote Sensing*, *44*, 3452–3461. doi:10.1109/Tgrs.2006.876297.

Zhang, K., Kimball, J. S., Nemani, R. R., & Running, S. W. (2010). A continuous satellite-derived global record of land surface evapotranspiration from 1983 to 2006. *Water Resources Research*, *46*. doi:10.1029/2009wr008800 Artn W09522.